MEASURING NEUTRAL SPECIES IN A PLASMA ENVIRONMENT USING DUAL COLOR SINGLE-SHOT COHERENT RAYLEIGH-BRILLOUIN SCATTERING

A Thesis

by

ROBERT T. RANDOLPH

Submitted to the Graduate and Professional School of
Texas A&M University
in partial fulfillment of the requirements for the degree of

MASTER OF SCIENCE

Chair of Committee,	Richard Miles
Co-Chair of Committee,	Alexandros Gerakis
Committee Member,	Waruna Kulatilaka
Head of Department,	Ivett Leyva

December 2021

Major Subject: Aerospace Engineering

ABSTRACT

Laser diagnostic methods provide a remote, non-perturbative way to accurately measure properties of gas and plasma flows such as velocity, density and temperature, leading to increased understanding of the properties of the flow and ultimately more efficient engineering designs. This work demonstrates the use of a non-linear, non-resonant four-wave mixing laser diagnostic technique known as single-shot coherent Rayleigh-Brillouin scattering (CRBS) to measure neutral density and translational temperature in a partially ionized plasma environment. Using a frequency doubled probe beam, CRBS spectra is obtained in gases and low-temperature plasmas of pressures down to 1-10 Torr. Diagnostics are performed in a xenon DC glow discharge due to its low ionization ratio. Using the CRBS laser system, translational temperature and neutral density are measured radially from the center to edge of the glow at a constant current and in the center of the glow with applied currents between 0-30 mA. Experimentally obtained spectra are compared to simulated spectra from the established Tenti s7 model to show agreement. Successful simultaneous density and temperature measurements in a partially ionized environment such as a glow discharge can help demonstrate the viability of single-shot CRBS in other plasma environments including arc discharges, combustion chambers, and hypersonic vehicles.

ACKNOWLEDGMENTS

Completion of this thesis and experimental work could not have been done without the help of numerous people. First and foremost, my advisors Dr. Alexandros Gerakis and Dr. Richard Miles provided countless pieces of advice, from formulation of the project to fine tuning the thesis and presentation. The project could not have been completed without Dr. Gerakis in particular, who designed the original single shot CRBS system and who taught me how to operate much of the CRBS system. The idea to evaluate CRBS measurements in a plasma environment was decided by Dr. Gerakis, while using a glow discharge was suggested by Dr. Miles. I would also like to thank Dr. Waruna Kulatilaka for serving as a committee member for my thesis and providing further insights on optics, both as part of the committee and in class.

Members of the Optical Probing and Manipulation (OPM) group, headed by Dr. Gerakis and which I am a part of, provided crucial help in completion of the project. In particular, Dr. Junhwi Bak, the post-doctoral researcher in the group, trained me and provided critical help and advice for data collection with the CRBS system. He also designed the original Labview and Matlab programs for data collection and analysis of CRBS spectra in gases, which I modified later to add features for use in plasmas. I would also like to thank Devin Merrell, an undergraduate in the group, who assisted in data collection with the glow discharge.

Of great importance to the project was Dr. Mikhail Shneider of the Mechanical and Aerospace Engineering Department at Princeton University. Dr. Shneider's theoretical work complements the CRBS experiments carried out by the OPM lab group. He also provided me with and taught me how to use the s7 simulation code used to compare simulated CRBS lineshapes with our experimental results.

Also of contribution to the project were lab staff John Kochan and Cecil Rhodes, who provided help setting up the laboratory work area, machining parts, and general advice related to mechanical and electrical systems. In addition members of the Bowersox group, Miles group and the LDPL group at Texas A&M allowed us to borrow equipment and helped to set up some experiments.

Of important contribution outside the lab were the administrative support staff of the Aerospace Engineering department including Colleen Leatherman, Julie Allen, Andrea Loggins and Brandi Bolin, who helped with purchasing and materials acquisition. I would also like to thank the Texas A&M University Graduate and Professional School for this LaTeX thesis template.

Last but perhaps most importantly, I would like to thank my family for supporting me in my graduate school pursuits, no matter how far from home they may be.

CONTRIBUTORS AND FUNDING SOURCES

Contributors

This work was supported by a thesis committee consisting of Professors Alexandros Gerakis and Richard Miles from the Department of Aerospace Engineering as co-advisors and Professor Waruna Kulatilaka of the Department of Mechanical Engineering as a committee member.

Using single-shot CRBS to diagnose neutral particles in plasmas was the idea of Dr. Gerakis while Dr. Miles suggested using a glow discharge as an initial source. The Tenti s7 code used to produce the modelled lineshapes in Chapters II and III was provided by Dr. Mikhail Shneider of the Department of Mechanical and Aerospace Engineering at Princeton University. The code was originally published in Ref. [1]. The laser setup described in section 2.2 was originally designed by Prof. Alexandros Gerakis and built with the help of Dr. Junhwi Bak and this student. Drs. Bak and Gerakis also assembled the LabVIEW and Matlab programs used to record and process the data from experiments measuring gas properties. Finally, Dr. Gerakis applied for and received grants to financially support the project.

All other work conducted for the thesis was completed by the student independently.

Funding Sources

This material is based upon work supported by the National Science Foundation under Grant No. 1903481 and Dr. Gerakis' startup funds.

NOMENCLATURE

LASER	Light Amplification by Stimulated Emission of Radiation
MASER	Microwave Amplification by Stimulated Emission of Radiation
TGV	Thermal Grating Velocimetry
KTV	Krypton Tagging Velocimetry
PLIF	Planar Laser Induced Fluorescence
VENOM	Vibrationally Excited Nitric Oxide Monitoring
FLEET	Femtosecond Laser Electronic Excitation and Tagging
CARS	Coherent Anti-Stokes Raman Spectroscopy
SRBS	Stimulated Rayleigh-Brillouin Scattering
CRBS	Coherent Rayleigh-Brillouin Scattering
FRS	Filtered Rayleigh Scattering
VDF	Velocity Distribution Function
EOM	Electro-Optic Modulator
$LiTaO_3$	Lithium tantalate crystal
Nd:YVO_4	Neodymium doped yttrium vanadate crystal
Nd:YAG	Neodymium-doped yttrium aluminum garnet
IEOM	Intensity Electro-Optic Modulator
LBO	Lithium triborate
FFT	Fast Fourier Transform
FWHM	Full Width Half Maximum
Ar	Argon

CO_2	Carbon dioxide
N_2	Nitrogen (molecular)
Xe	Xenon
η	Coupling efficiency
ϵ_0	Permittivity of free space
μ_0	Permeability of free space
c	Speed of light
h	Planck constant
k	Boltzmann constant

TABLE OF CONTENTS

Page

LIST OF FIGURES

FIGURE Page

1. INTRODUCTION TO LIGHT SCATTERING

1.1 Scope

There is a need in the aerodynamic and experimental fluid dynamic communities for accurate measurement techniques in gas and plasma environments. In addition to better understanding gas and plasma flows, diagnostics are necessary to aid in the design of a variety of aerospace projects both in the public and private sectors. For instance, temperature and density flow diagnostics are needed to make gas turbine engines more thermally efficient while also providing higher thrust [4], reducing drag and increasing stability of supersonic and hypersonic vehicles [5], and studying the output from experimental propulsion techniques such as Hall thrusters [6]. Traditional temperature and pressure diagnostic methods such as thermocouples and pitot tubes are not ideal for these environments because their presence may cause disturbances in the flow, such as producing shock waves in the supersonic regime [5]. Sample species may also react with the equipment, further impacting the flow plus potentially damaging equipment [7]. To negate this problem, researchers have designed a variety of laser diagnostic methods to use in these environments because they have the potential to be non-intrusive and remote. However, there is still a need for additional rapid laser diagnostic techniques to measure properties of neutral particles in low pressure, optically noisy plasma environments. This work will demonstrate the use of a non-linear four wave mixing laser diagnostic technique known as single-shot coherent Rayleigh-Brillouin scattering (CRBS) to measure temperature and density of neutral particles in gaseous and partially ionized plasma environments. A DC glow discharge is used for the plasma environment due to its low ionization ratio ($10^{-6} - 10^{-4}$) [8], allowing measurements of primarily neutral particles. CRBS will be used to simultaneously measure neutral density and translational temperature. Demonstrating CRBS in a DC glow discharge will assist in proving the viability of the technique in more complex plasma environments such as in combustion chambers or propulsion systems.

1.2 A Historical Introduction to Optical Scattering and the Dual Nature of Light

A brief look at some of the major achievements throughout history in the field of optical scattering is important to understand the background behind CRBS. Written accounts on the nature of light have been found as far back as the ancient Greeks with writings by Empedocles and Euclid around 450 and 300 BC [9, 10]. Most of the work at these times were speculations as to the nature of light based on observations of burning lenses, refraction, reflection, and light propagation.

As the understanding of light grew, two schools of thought developed over whether light was composed of particles or waves. In 1637, the philosopher René Descartes put forth the idea of a corpuscular theory of light, stating that light was made of many microscopic particles [11]. At the same time, he also made observations on the refraction of light, or how the angle of light changed between media, which formed the basis of Snell's law. In 1672, the famed physicist Isaac Newton expanded on this work which was later published in his book *Opticks* in 1704 [12]. In addition to stating that light was made of small particles, Newton said that those particles obeyed the same laws of physics as larger objects and that the particles are small enough to avoid scattering off of each other. This theory attempted to explain refraction by stating light particles experience different forces of attraction to different media based on density, thus at boundary layers unequal forces would cause a change in velocity. Between water and air for instance, the light particles would speed up in the direction normal to the boundary layer as they approach water, accounting for the observed change in angle relative to the normal of the surface. Newton also used his theory to explain how different colors form. He believed light of different colors had different masses, which would account for different angles each color takes when separated in a prism. Newton's theory could also explain polarization, which was originally documented in 1669 by mathematician Erasmus Bartholinus, by stating that light particles are nonspherical shapes meaning only particles oriented in a certain position could pass through a polarization filter [13].

Mainly due to Newton's status at the time, the corpuscular theory of light was generally favored over the wave theory. The corpuscular theory of light however had several limitations including the inability to explain several phenomena well known at the time such as interference and diffraction.

A major blow to the corpuscular theory came in 1850 when both Hippolyte Fizeau and Léon Foucault independently determined the speed of light in water to be less than the speed in air [14], proving Newton's corpuscular theory of light wrong. According to Newton's theory, the light must speed up in water relative to air, meaning some other phenomena is responsible for refraction.

Contributions establishing the wave theory of light began in 1665 when the physicist Francesco Maria Grimaldi observed light diffraction and noticed light's wavelike behavior [15]. The theory was popularized however by mathematician Christian Huygens later in 1678. Huygens stated that light was composed of waves which propagated perpendicular to the direction of movement. In what became known as Huygens' principle, he stated that every point on a wavefront acts as a source of spherically propagating wavelets. With his theory, Huygens successfully explained reflection and refraction, but was unable to explain diffraction effects. He later published much of his findings in 1690 in his book *Traite de la Lumiere* [16]. These contributions unfortunately were overshadowed for many years after their conception by Newton's corpuscular theory of light.

Thomas Young in 1801 brought wave theory back into prominence with the double slit experiment [17]. By shining a light through two equally sized slits and observing an interference pattern behind the slits, he concluded light exhibits wavelike properties. Young also later calculated the wavelength of light to be less than 1 μm. In 1815 engineer and physicist Augustin-Jean Fresnel derived equations to more fully explain the double slit experiment according to the wave theory of light [18, 19]. Earlier in 1805 Fresnel had derived equations related to light interference and hypothesized visible light was composed of very small wavelengths [19]. The mathematician Siméon Denis Poisson originally believed Fresnel's calculations were wrong because they predicted a bright spot at the center of a shadow cast from an opaque disk, an impossibility according to the corpuscular theory of light. To test the calculations, physicist Francois Arago performed a series of experiments showing that, when certain conditions are satisfied, the bright spot does indeed occur [20]. This spot became known as the Arago spot or, ironically, the Poisson spot. These studies brought the wave theory of light back into prominence, however the theory still left unexplained phenomena.

Between 1861 and 1862 mathematician James Clerk Maxwell developed a series of equations, later to be known as Maxwell's equations, to describe the propagation of electromagnetic waves [21, 22]. A major assertion stemming from the Maxwell equations is that electromagnetic waves move at a constant speed (c) in a vacuum [23]. The Maxwell equations relate electric fields to magnetic fields and are as follows:

$$\nabla \cdot \mathbf{E} = \frac{\rho}{\epsilon_0}, \tag{1.1a}$$

$$\nabla \cdot \mathbf{B} = 0, \tag{1.1b}$$

$$\nabla \times \mathbf{E} = -\frac{\delta \mathbf{B}}{\delta t}, \tag{1.1c}$$

$$\nabla \times \mathbf{B} = \mu_0 \mathbf{J} + \mu_0 \epsilon_0 \frac{\delta \mathbf{E}}{\delta t}. \tag{1.1d}$$

Earlier experiments conducted by Rudolph Kohlrausch and Wilhelm Weber found the speed of an electromagnetic signal to have a constant velocity of approximately $3 \cdot 10^{-8}\mathrm{m/s}$, which was nearly equal to the speed of light experimentally determined earlier by Fizeau and Foucault [24]. These findings led Maxwell to believe light was also an electromagnetic wave with a constant velocity. In 1888, Heinrich Hertz proved through a series of experiments that the speed of light is equal to the speed of other electromagnetic waves, supporting Maxwell's theory [25]. As much as Maxwell's equations allowed physicists to better understand visible light and electromagnetic radiation in general, they however still failed to describe light emission and absorption, including dark lines in the solar spectra observed by Joseph von Fraunhofer in 1814 [26].

The discovery of quantum mechanics brought a deeper understanding of optics including many forms of light scattering. In 1900, the physicist Max Planck derived what became known as Planck's law to explain the observed radiation spectra emitted from blackbodies, including the dark spots observed earlier in the solar spectra [27]:

$$B_\lambda(T) = \frac{2hc^2}{\lambda^5} \frac{1}{e^{\frac{hc}{kT\lambda}} - 1}. \tag{1.2}$$

Here Planck hypothesized that energy is emitted from blackbodies in discrete amounts, which became known as quanta. This work was published in 1901 in *On the Law of Distribution of Energy in the Normal Spectrum* [28]. In 1905, Albert Einstein further explained Planck's theory by proposing a particle theory of light once again. In the first of several groundbreaking papers dubbed the *Annus mirabilis* papers, he theorized that light is made of tiny particles known as photons which travel as a wave [29]. These photons have an energy proportional to their frequency given by the equation Planck had earlier derived:

$$E = \hbar f. \tag{1.3}$$

Prior to Einstein's theory in 1887, Heinrich Hertz noticed that shining a beam of light at a piece of metal would cause the metal to emit electrons, which created sparks visible to an observer. Hertz noticed that different metals required different frequencies of light before they began to emit electrons [30], however he could not explain the reason. Of note to Hertz's observations was that the frequency of the light must be changed, not the intensity, to emit electrons. Einstein hypothesized that a single photon must reach or exceed a certain threshold energy to eject a single electron from the metal [31]. This became known as the photoelectric effect and was the reason Einstein was awarded the 1921 Nobel Prize in Physics, despite him being more well known at the time for his theory of relativity.

These discoveries have shaped the modern day view of the dual nature of light. As seen in the following chapters, many light scattering phenomena and laser diagnostic methods including CRBS are dependent on both the wavelike properties of light, such as interference, and on the particle nature of light including the exchange of energy between neutral molecules and photons.

1.3 Light Scattering

Light scattering is collection of naturally occurring phenomena that occurs as photons interact with particles in a medium. By analyzing spectra of the scattered light, information on the particles such as temperature, velocity, and species may be obtained. Although light had been investigated

for many years before, light scattering was first studied extensively in 1869 when John Tyndall discovered that light scattered off of particles in a gas or liquid suspension emitted a blue hue. This became known as Tyndall's effect [32, 33]. Although he could not explain why light emitting blue wavelengths was favored, he hypothesized that this phenomenon also caused sunlight to turn the sky blue. Two years later, in 1871, John William Strutt (better known as Lord Rayleigh) provided a mathematical explanation to Tyndall's effect [34], specifically finding that the intensity of the scattering is proportional to λ^{-4}, where λ is the wavelength of the incoming light beam. Since Tyndall's observations, a variety of scattering phenomena have been studied.

Most types of scattering are classified based on the energy levels of the particle before and after scattering takes place. In all cases, the classical theories of conservation of energy and momentum may be applied to model the scattering at the atomic level, meaning the total energy of the system (photons and particles in the medium) remains the same before and after scattering, although energy may be transferred between particles and photons. Types of light scattering may be classified into two types as seen in Fig. 1.1: elastic (in which the total kinetic energy of the system is conserved and particles remain at the same energy level) or inelastic (where the energy level of the particles changes). Inelastic scattering is further classified into Stokes and anti-Stokes scattering

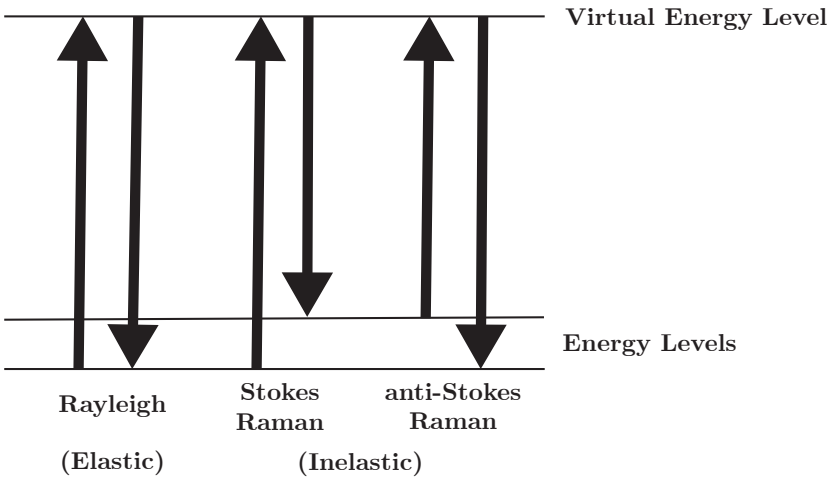

Figure 1.1: Illustration of movement between molecular energy levels for Rayleigh scattering, an elastic scattering method, and Stokes and anti-Stokes Raman scattering, both inelastic methods.

depending on if the molecule moves to a higher or lower energy level, respectively. As a result, the energy and thus the wavelength of the photon also changes, with Stokes scattering causing a red shift in the light while anti-Stokes causes a blue shift.

1.3.1 Rayleigh Scattering

Perhaps one of the most well studied forms of scattering, Rayleigh scattering was first described by John William Strutt (Lord Rayleigh) in a series of papers culminating in relating the intensity of the scattering to the polarizability of the molecules in the medium [35]. Rayleigh scattering is a result of photons being dispersed from particles in a medium moving with randomized thermal motions. The scattering can occur in both atoms and molecules, as long as the size of the particles is much less than the photon's wavelength. As the size of the particle increases or the ratio of the diameter of the particles to the wavelength of the incident light approaches one, the scattering is known as Mie scattering [36]. Modelling the scattering in this regime requires additional equations to account for the interference patterns produced from the larger particle size. Beyond Mie scattering, particles much larger than the wavelength of the incident light scatter light according to their geometric shape, moving into the field of geometric optics.

During Rayleigh scattering, as photons scatter off particles moving with different velocities, the wavelengths of individual photons change due to Doppler broadening. The change in frequency of a single photon when hitting a particle with velocity v relative to the observer for non-relativistic velocities is given by:

$$f = f_0(1 + \frac{v}{c}). \tag{1.4}$$

The thermal motion is random and follows a Gaussian distribution, giving a probability distribution of:

$$f(v_z) = \sqrt{\frac{m}{2\pi kT}} e^{\frac{-mv_z^2}{2kT}}. \tag{1.5}$$

Since the motion of particles is random, the average energy change among all photons equals zero, meaning Rayleigh scattering is an elastic process. Following Eqn. 1.5, as temperature (T) increases, the translational velocity of the molecules increases creating a broader Doppler shift.

The intensity of Rayleigh scattering is given by:

$$I = I_0 \frac{8\pi^4 N\alpha^2}{\lambda^4 R^2}(1 + cos^2\theta). \tag{1.6}$$

Of note is that the intensity is proportional to λ^{-4}, the same relationship Lord Rayleigh used to explain Tyndall's effect as mentioned earlier. Consequently, Rayleigh scattering is more pronounced at shorter light wavelengths, which is responsible for giving the sky its bluish hue during the day. The intensity also depends on the polarizability of the medium as mentioned earlier, meaning gases such as xenon with higher polarizability produce a stronger signal.

1.3.2 Brillouin Scattering

Named after Léon Brillouin who in 1922 predicted inelastic light scattering [37], Brillouin scattering arises from the change in refractive index of a medium due to periodic perturbations, or waves in said medium. From a quantum perspective, the photons either absorb or emit energy corresponding to the speed of the wave. This packet of energy may be thought of as a quasiparticle, such as a phonon in the case of acoustic waves, transferring between the medium in the wave and the photon [38]. Due to this change in energy, the scattering is considered inelastic.

In a gaseous medium, such as in the experiments presented here, the shift in energy for Brillouin scattered photons is proportional to the speed of perturbations in the medium, or the speed of sound. The change in photon energy corresponds to a change in wavelength or frequency of the light, which manifests itself as a shift in the location of the Brillouin peaks in both the positive and negative directions from the center of the signal spectrum, where the Rayleigh peak is centered. Converting from the frequency to the velocity domain presents the shift in units of velocity instead of frequency, the velocity difference which equals the Mach speed in the medium. As the name suggests, Brillouin scattering is one of the scattering types of interest in CRBS along with Rayleigh scattering.

1.3.3 Raman Scattering

Another form of inelastic scattering affecting neutral particles is Raman scattering. First discovered in 1928 by Sir Chandrasekhara Venkata Raman [39], Raman scattering involves a shift in photon energy equal to a shift in molecular vibrational energy. Since it relies on the molecular vibrational energy, Raman scattering may only occur in molecules, not atoms, with the exception of hydrogen due to it having different spin isomers. For Raman scattering to occur, an incident photon collides with a molecule in the medium, moving the molecule to a higher virtual energy level equal to its original energy level plus the energy of the incident photon. A new photon is emitted with a different magnitude of energy compared to the original photon, lowering the energy level of the molecule from the virtual state to an energy level it was not at prior to the collision. Due to Eqn. 1.3, the frequency of the photon is also changed.

Since the change in energy level of the photon corresponds to the change in energy of the molecule, calculating the change in energy as the molecule moves between vibrational energy levels can predict the change in photon energy. To find the change in energy level, individual molecules in the medium may be approximated as quantum harmonic oscillators with vibrational energy levels given by [40]:

$$E_n = h(n + \frac{1}{2})\frac{1}{2\pi}\sqrt{\frac{k}{m}}. \tag{1.7}$$

In the equation, n is a positive integer representing the energy level. Therefore, jumping to the next highest energy level, as is typical for Stokes Raman scattering, results in the following change in energy of the molecule and thus the same (but opposite in magnitude) change between the incident and scattered photon:

$$E = \frac{h}{2\pi}\sqrt{\frac{k}{m}}. \tag{1.8}$$

By combining Eqns. 1.8 and 1.3, the change in frequency from the incident light may be determined. Vibrational and rotational temperature of particles in the medium may be measured based on the ratio in intensity between the Stokes and anti-Stokes spectra. Additionally, the species in the medium may be determined from the shifts in frequency, which occur at magnitudes unique

for different molecular species.

1.3.4 Other Types of Scattering

The previously mentioned scattering types involved photons scattering off of neutral particles. Other classifications of light scattering exist to address scenarios when the particle is charged (such as if a photon scatters from an electron) including Compton and Thomson scattering. Thomson scattering is the elastic scattering of photons from charged particles, typically electrons while Compton is inelastic. The photon energy must be much less than the mass energy of the particle for these techniques to occur. Thomson scattering is nonrelativistic while Compton is relativistic [40].

1.4 Laser Diagnostic Methods

In 1954 Charles Townes created a device which amplified microwaves at 24 GHz using stimulated emission from ammonia molecules [41]. The device was dubbed the maser, an acronym for microwave amplification by stimulated emission of radiation. From this arose the first laser (standing for Light Amplification by Stimulated Emission of Radiation), developed in 1960 by Theodore Maiman. This device was flashlamp-pumped and used a ruby crystal to emit light at 694 nm [42, 43]. The birth of laser diagnostics soon followed as physicists used lasers to stimulate various types of light scattering [44]. Described here are several notable laser diagnostic methods and their relationship to single-shot CRBS. Techniques are broken into categories including resonant or non-resonant, seeded or unseeded, and coherent or non-coherent.

Prior to lasers, techniques including Rayleigh and Raman scattering could only be spontaneous, meaning scattering occurs at random intervals as particles in higher energy states decay to lower states. As a result, only weak signals could be detected, requiring sampling intervals lasting hours or even days to view a single spectrum. The advent of lasers allowed for stimulated laser diagnostic techniques, where incoming photons could excite, or stimulate, the particle causing it to release a photon and drop an energy level [44]. It is important to note that a similar stimulation process occurs in lasers causing light amplification, however the focus here is on the stimulation of particles in gas or plasma media in a testing environment, not within the laser itself. Many modern laser

diagnostic techniques use stimulated emission within the medium under study due to the higher intensity signal produced.

1.4.1 Resonant versus Non-resonant

Resonant techniques require the laser wavelength to correspond to the change in energy level of the species under study. This required laser wavelength is commonly referred to as the resonance frequency. These techniques include coherent anti-Stokes Raman spectroscopy (CARS) [45, 46, 47, 48, 49], Femtosecond Laser Electronic Excitation and Tagging (FLEET) [50, 51, 52, 53], thermal grating velocimetry (TGV) [54], krypton tagging velocimetry (KTV) [55, 56, 57], planar laser induced fluorescence (PLIF) [58, 59, 60], particle image velocimetry (PIV) [61, 62], and vibrationally excited nitric oxide monitoring (VENOM) [63, 64, 65]. Measurements with some resonant techniques allow determination of the type of species present in a sample as well as the ratios in amounts of those species if multiple are present. This is possible because different molecular species have different energy levels, thus different resonance frequencies. To detect the properties of different species however, the laser must be tuned to the specific resonant wavelengths for those species.

Coherent anti-Stokes Raman spectroscopy, or CARS, is one such non-linear, resonant laser diagnostic technique. This technique uses three pulsed beams, a pump beam (ω_p), Stokes beam (ω_s), and probe beam (ω_{pr}). The interaction of these beams produces a fourth coherent signal beam of frequency $\omega_{pr} + \omega_p - \omega_s$, as seen in Fig. 1.2. If the difference in frequency of the pump and Stokes beam ($\omega_p - \omega_s$) matches an anti-Stokes Raman resonance frequency of the sampled media, the signal is resonantly enhanced. This provides the capability to determine the species present in a sample as well as the vibrational temperature [66].

Non-resonant techniques meanwhile use signal beams of frequencies far from the resonant frequency of the gases in the medium, meaning the signal spectrum is influenced by all the particles in the medium, not just from a specific species. This may either be an advantage or disadvantage depending on the application. For instance, setups do not need to be tuned to a different wavelength to scatter from a new species. However, non-resonant techniques may not be able to isolate specific

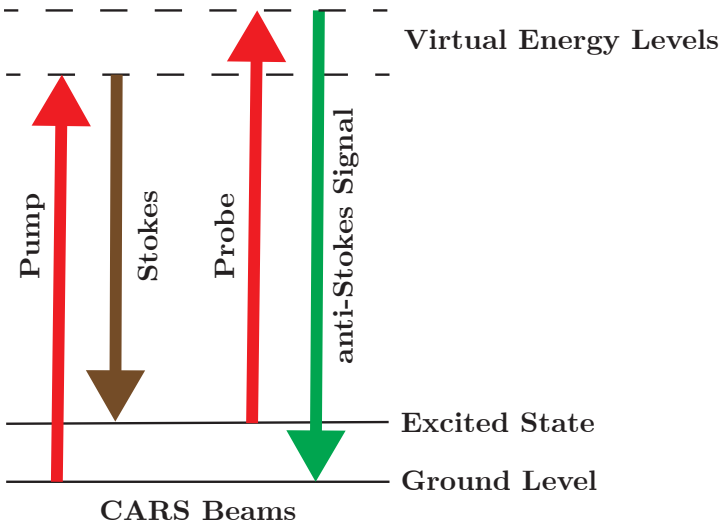

Figure 1.2: Depiction of the change in molecular energy level during CARS. Occuring first is a rise in molecular energy to a virtual energy state with the pump beam, then a drop to the excited state with the Stokes beam, followed by another rise to the second virtual energy state, then finally the emission of the signal beam causing the molecule to fall to the lowest, original energy state.

species in a media or identify which species are present. Filtered Rayleigh scattering (FRS) [67], stimulated Rayleigh-Brillouin scattering (SRBS) [68, 69], and coherent Rayleigh-Brillouin scattering (CRBS) [70, 1] are all non-resonant techniques.

SRBS, FRS and CRBS are concerned with Rayleigh and sometimes Brillouin scattering. The difference in intensities between the two types of scattering is characterized by the y-parameter, which is proportional to the ratio between the grating wavelength and the mean free path of the gas:

$$y \propto \frac{N_0 k_B T}{k \eta \upsilon_0}. \tag{1.9}$$

As y approaches zero, Rayleigh scattering is dominant causing the spectrum of the scattered light to approximate a Gaussian curve. This is known as the Knudsen regime. As y-parameter values approach one or above, the medium enters the kinetic regime and Brillouin scattering becomes noticeable causing two shifted peaks to form centered on frequencies in the spectrum domain corresponding to the speed of sound of the medium. The medium is in the hydrodynamics regime,

where Brillouin peaks begin to dominate the spectrum, if the y-parameter is above 3 [71].

The simplest of the aforementioned non-resonant techniques is SRBS, which uses a laser beam to stimulate particles in a medium then spectrally analyzes the scattered signal. Since SRBS is elastic or non-resonant, the signal can contain stray elastic optical noise making spectra not well defined. FRS, the next non-resonant technique, improves upon SRBS by using a resonant atomic vapor filter to remove this noise, allowing measurement of a cleaner signal [67]. The final non-resonant technique, CRBS, is described in detail later.

1.4.2 Seeded versus Unseeded

Seeded diagnostic methods inject a specific gas into a flow which fluoresces when colliding with photons from the laser beam probing the sample. Essentially, particles of the seeded gas species have a resonance frequency matching the laser beam frequency, allowing the particles to jump to different energy levels. Primarily used to measure velocity in a flow, these techniques are resonant and include TGV, KTV, PLIF, PIV and VENOM as introduced previously. These laser diagnostic methods may increase the signal intensity due to the seeded particles, however they may inadvertently affect properties of the flow due to the introduction of additional gases. These techniques assume that the seeded gas holds the same properties as the rest of the flow, an assumption which may not be true in plasma environments. Unseeded techniques in contrast do not require additional particles to be added to the flow field.

1.4.3 Coherent versus Non-coherent

The terms coherent and non-coherent refer to how the resulting signal is scattered from the medium. Non-coherent techniques scatter the signal in a 4π angle. In other words, photons are randomly dispersed in all directions after colliding with particles in the medium. These techniques include SRBS, FRS, KTV, PLIF, VENOM and FLEET as mentioned earlier, among others. In most cases, detection equipment must be close to the measurement location in order to obtain a strong signal. Optically noisy environments may also prevent an accurate signal from being obtained.

Coherent techniques produce a signal beam through phase-matched Bragg scattering which

remains approximately the same intensity as the beam moves away from the measurement location. CRBS and CARS are both coherent laser diagnostic techniques. For coherent scattering to occur, Bragg's law must be followed which states that the difference in path length of light scattered from different layers of a lattice is equal to an integer multiple of the wavelength. This is mathematically described by the equation:

$$n\lambda = 2dsin(\theta), \tag{1.10}$$

where λ is the wavelength of the incoming light, d is the distance between the gratings, θ is the angle of incidence, and n is an integer specifying the order of the scattering. Since the particles scattering from the lattice are phased matched assuming the angle of incidence follows Eqn. 1.10, constructive interference occurs causing a strong beam. As opposed to a signal radiating in a 4π solid angle, which has a signal strength proportional to r^{-2} where r is the distance from the measurement location, coherent techniques experience little loss in signal strength with distance r. This is beneficial in increasing the signal to noise ratio because optical noise still scatters in a 4π solid angle and decreases proportional to r^{-2}, as mentioned previously. As a result the signal to noise ratio of the measured spectra is higher the further the measurement is assessed from the probing location. Besides increasing the signal to noise ratio, remote measurement locations also help keep equipment such as photodiodes safe and avoid interference with the path of the flow.

1.5 Coherent Rayleigh-Brillouin Scattering

Coherent Rayleigh-Brillouin scattering or CRBS is a nonlinear four-wave mixing technique where two pulsed beams, known as the pumps, intersect to form an optical interference pattern or grating [1, 71]. The pump beams, which have equal wavelength λ_{pump} and the same polarization, are aligned with a crossing half-angle of $\Phi/2$, which is typically between $85°$-$89°$. Although in theory $90°$ would be the ideal crossing half angle, in practice this alignment is avoided to prevent damage to equipment due to optical feedback.

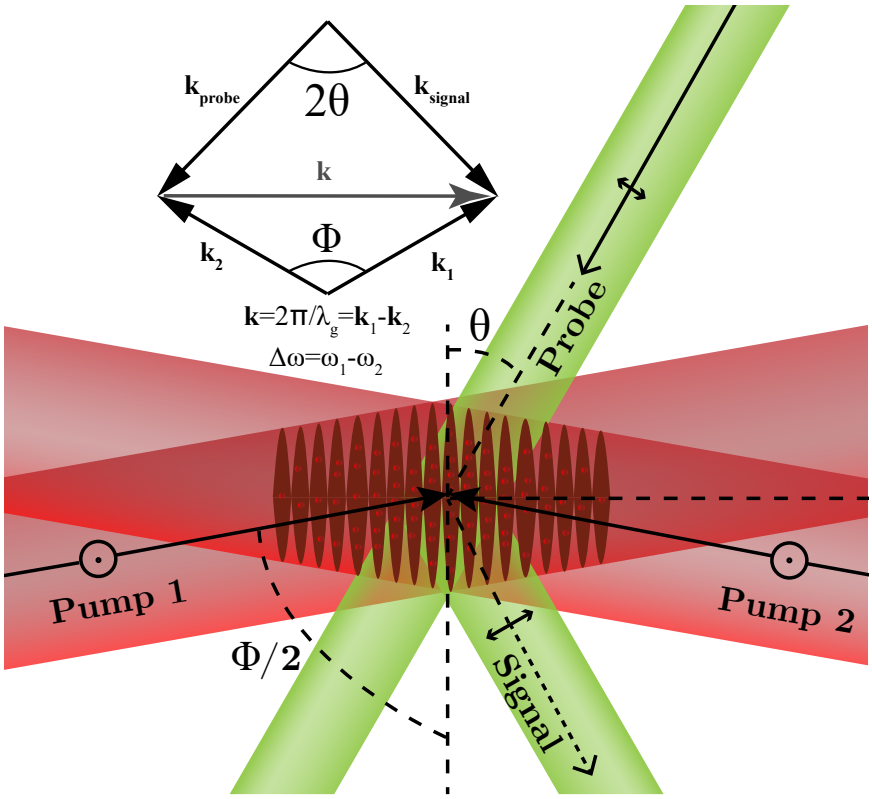

Figure 1.3: Close up depiction of the measurement region for CRBS. Two pump beams intersect forming an optical gradient, which induces particles in the medium to form a lattice. A probe beam then Bragg scatters from the lattice forming a coherently scattered signal beam.

The wavelength of the optical grating, λ_g, is given by the equation:

$$\lambda_g = \lambda_{pump}/(2 \cdot sin(\phi/2)), \tag{1.11}$$

where λ_{pump} is the wavelength of the pumps and $\phi/2$ is the crossing half-angle. The optical grating pattern moves at a phase velocity, υ_g, given by the equation:

$$\upsilon_g = (\Delta f \cdot \lambda_{pump})/(2 \cdot sin(\phi/2)). \tag{1.12}$$

Of note is that Δf, the frequency difference between the two pumps, is directly proportional to the lattice velocity. The potential energy in this region is given by the equation:

$$U = \frac{1}{2}\alpha_{eff}\left|E^2\right|, \tag{1.13}$$

where α is the polarizability and E is the electric field. Changes in the electric field, and consequently the potential energy, result in an optical dipole force affecting particles in the medium given by:

$$F_{OD} = -\nabla U = \frac{1}{2}\alpha_{eff}\nabla\left|E^2\right|. \tag{1.14}$$

As a result, particles in the medium with translational velocities υ roughly equal to the phase velocity υ_g move towards high intensity regions of the optical interference pattern, creating a lattice structure, as seen in Fig. 1.3.

A third beam, known as the *probe*, intersects the lattice structure at a specific angle creating a coherently scattered beam known as the signal. To produce this coherently scattered signal beam, the angle θ of the probe beam incident to the induced optical lattice fulfills the first order Bragg condition, given by:

$$\lambda_{probe} = 2\lambda_g \cdot sin(\theta). \tag{1.15}$$

Combining and rearranging Eqns. 1.11 and 1.15 gives:

$$\theta = sin^{-1}(\frac{\lambda_{probe} sin(\phi/2)}{\lambda_{pump}}), \tag{1.16}$$

in which θ is the Bragg angle as depicted in Fig. 1.3. The probe beam is polarized orthogonally in relation to the pumps to allow a thin film polarizer to separate the generated signal beam from the pumps since the signal has the same polarization as the probe (i.e. orthogonal to the pumps). This is particularly important when the probe and pump beams share the same wavelength. The intensity of the signal is given by equation:

$$I_S \propto L^2(\Delta N)^2 I_1 I_2 I_{pr} \propto \Delta n^2, \tag{1.17}$$

and is proportional to the square of the induced refractive index modulation Δn. The refractive index modulation is caused by the polarizability of the medium and is given by the relation [3]:

$$\Delta n \propto \alpha_{eff}^{2-2.5}. \tag{1.18}$$

As a result, signal intensities are higher in media with higher polarizabilities. Signal intensities are also higher when more particles are captured by the lattice. The velocity distribution function (VDF) gives the probability distribution of particles moving at a range of velocities in a medium. While sweeping through a range of Δf values, and consequently a range of υ_g values, those υ_g values that capture more particles in the lattice result in higher signal intensities at that velocity value on the spectrum, thus scanning the VDF.

Rather than manually changing the wavelengths of one or both pump beams to obtain new Δf values, a chirped frequency may be used to rapidly scan the VDF. First applied to CRBS in 2013 [72], this technique, henceforth referred to as the single-shot technique, utilizes one pump beam of constant frequency and another with a chirped frequency, scanning the entire VDF in the span of hundreds of nanoseconds as opposed to minutes. This is explained further in Sects. 2.2.1 and 2.2.2.

Similar to SRBS, a CRBS spectrum is a combination of a Rayleigh peak as well as two Brillouin peaks, the size of each peak dependent on the y-parameter as given in Eqn. 1.9. A breakdown of a sample CRBS spectrum is given in Fig. 1.4.

Finding the temperature of particles at the measuring point requires fitting the Rayleigh peak to the equation [70, 1, 71]:

$$f(v_z) \propto e^{\frac{-mv_z^2}{2kT}}. \tag{1.19}$$

This is a simplification of Eqn. 1.5. Knowing the atomic mass *m* of the particles relates the

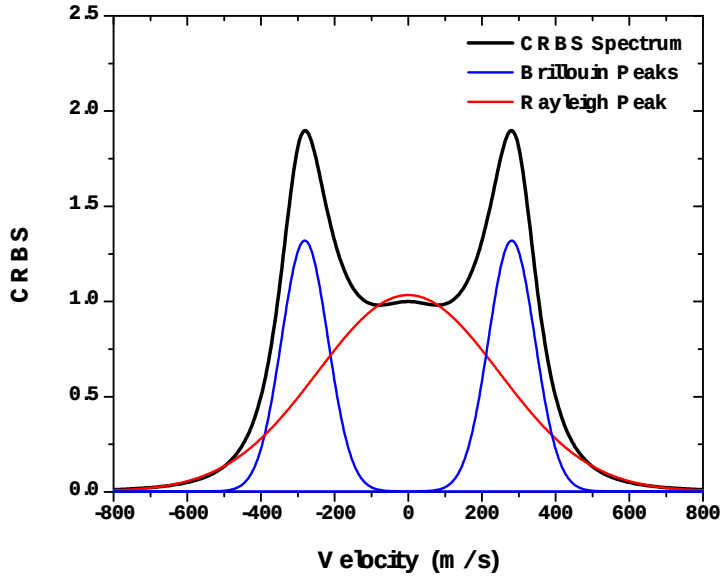

Figure 1.4: Example CRBS spectrum generated with the s7 model for CO_2 at 760 Torr. The components of the spectrum, the Rayleigh peak (red) and two Brillouin peaks (blue) are separated using a multipeak fit to visualize the contributions of each peak on the final spectrum.

temperature T to the width of the lineshape and allows fitting of the lineshape with T as the only variable.

The temperature may also be related to the full width half maximum value of the lineshape at low y-parameters if the Rayleigh peak is dominant. As previously mentioned, the Rayleigh peak may be approximated as Gaussian, the general Gaussian equation given by:

$$f(x) = \frac{1}{\sigma\sqrt{2\pi}} exp\left[-\frac{(x-x_0)^2}{2\sigma^2}\right]. \tag{1.20}$$

From the general Gaussian distribution, the full width half maximum is given by the following equation which may be related to temperature by setting $\sigma = \sqrt{\frac{kT}{m}}$, as is done in Eqn. 1.5:

$$FWHM = 2\sqrt{2ln2}\sigma \propto \sqrt{\frac{kT}{m}}. \tag{1.21}$$

From Eqn. 1.17, the relation between intensity and neutral density is found to be:

$$I_S \propto \Delta n^2. \tag{1.22}$$

The component of the average translational velocity of the medium along the optical lattice may also be determined by the shift of the spectra from the center, although this is not studied in this work.

Diagnostics in media with higher y-parameters allows viewing of the Brillouin peaks, which allow interpretation of more information about the media. As previously mentioned, Brillouin scattering is most intense at the offsets corresponding to the speed of sound in the medium. Thus viewing the optical spectrum in the velocity domain yields Brillouin peaks at the speed of sound or Mach speed. The speed of sound in gas has long been known [73], and is given by the following equation where *c* is the Mach speed, *T* is temperature, *m* is molecular mass, and γ is the adiabatic index:

$$c = \sqrt{\frac{\gamma kT}{m}}. \tag{1.23}$$

As a result, the change in location of the Brillouin peak is related to temperature by:

$$v_{\text{Brillouin}} \propto T^{-\frac{1}{2}}. \tag{1.24}$$

Knowing this allows determination of the Mach speed in the medium. If the gas species and initial temperature is known, the measured Mach speed and theoretically predicted speed may be compared to ensure the velocity domain of the CRBS spectrum is accurate. This comparison helps to ensure accurate temperature values are also measured.

2. GAS MEASUREMENTS WITH CRBS LASER SYSTEM

2.1 Motivation

Initial measurements in a gaseous environment are necessary to characterize the performance of the CRBS system before making measurements in plasmas, which typically have lower pressures and higher temperatures. This characterization includes how well defined the acquired spectra are at various temperatures and pressures and if they follow the Tenti s7 model. As such, this series of experiments obtains measurements in a wide range of pressures and temperatures and with several gas species. Obtaining the measurements in gas and eventually in plasma requires a high signal to noise ratio. In order to produce a strong signal to noise ratio, a well defined lattice must be produced along with a strong probe beam. A rapid acquisition time is also desirable for measurements, necessitating a single-shot setup to induce a rapid change in the lattice velocity and thus rapidly scan the VDF.

2.2 Laser System Setup

A laser system is needed to satisfy the performance requirements outlined above. This project uses the same single-shot CRBS setup discussed in greater detail in past literature [74, 75, 76]. The current system, designed and built at Texas A&M University, is a revision upon past systems built elsewhere [2, 3, 77]. The Texas A&M laser system is capable of producing two pump beams of pulse energies near 400 mJ to produce the optical interference pattern and thus the lattice structure. These pump beams also produce a probe beam of $30 - 40$ mJ. This is an improvement from past systems where pump beams had pulse energies up to only 200 mJ. In addition, the probe beam on this system is frequency doubled to 532 nm whereas in past systems the probe beam remained at 1064 nm, the same wavelength as the pumps. The system is also capable of producing a frequency chirp in a time frame as low as 100 ns with minimal oscillations, similar to past setups. The major components of the setup are briefly described here.

2.2.1 Master-Slave Injection Seeding

The rapid change in δf of the pump beams necessary for single-shot CRBS as described in Sect. 1.5 requires one pulse beam with a constant, stable frequency and another with a precise, chirped frequency. To satisfy these requirements, a master-slave injection-seeded laser configuration is used.

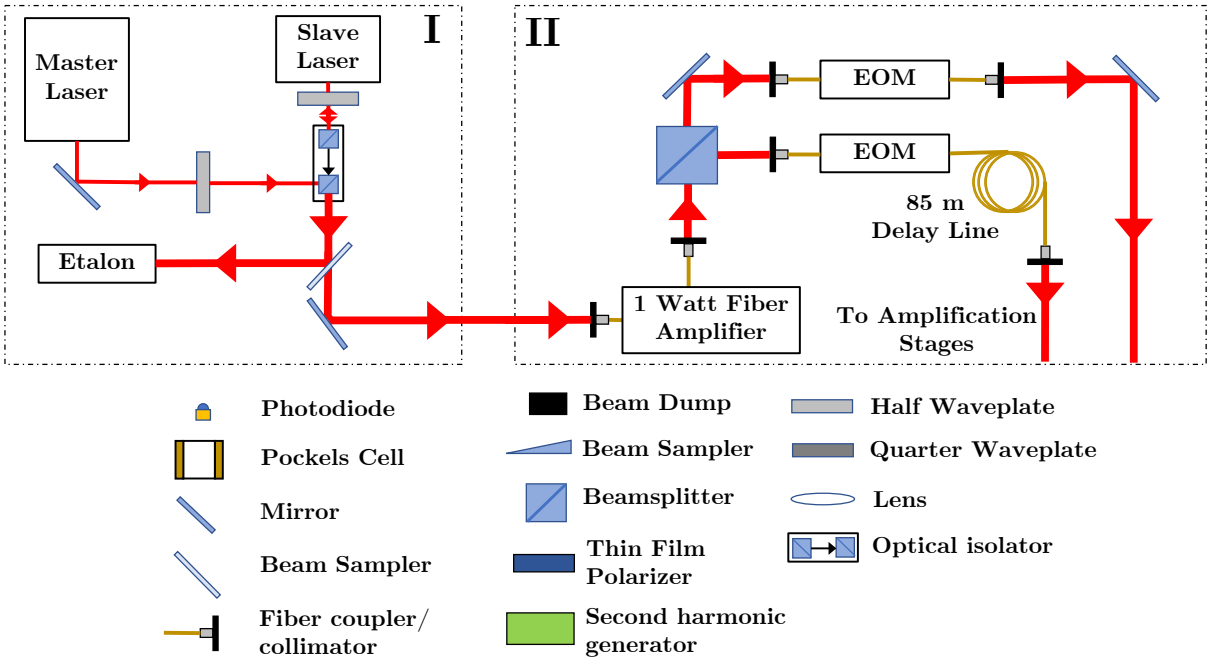

Figure 2.1: Schematic of parts I and II of CRBS setup. Part I details the equipment used for master-slave injection seeding in Sect. 2.2.1 while part II details the equipment used for pulse shaping in Sect. 2.2.2. Note that same legend is used in Figs. 2.3 and 2.9 to outline sections III and IV.

The laser output begins with the *master laser*, as depicted in part I of Fig. 2.1. This is a custom-built laser system consisting of an 808 nm pumping diode and laser cavity. The laser diode[1] pumps the active lasing medium, a Nd:YVO_4 laser crystal. After the lasing medium comes the laser cavity, which houses a $LiTaO_3$ electro-optic modulator (EOM) crystal. The EOM crystal alters the output frequency of the laser proportional to an applied voltage given by the equation [78]:

[1]Thorlabs L808P1000MM

$$\delta f = \frac{\eta \cdot n_1^2 \cdot r_{32} \cdot f_{opt}}{2 \cdot d} \frac{n_1 \cdot l_1}{n_1 \cdot l_1 + n_2 \cdot l_2 + n_3 \cdot l_3} \delta V. \tag{2.1}$$

As voltage is applied to the EOM, the laser cavity length changes due to a change in the refractive index of the crystal, which causes the change in laser frequency as seen in Fig. 2.2. Other variables include the coupling efficiency η between the electric field and the laser cavity mode; the lengths of the $LiTaO_3$ crystal l_1, the Nd:YVO_4 crystal l_2, and the air gap l_3; the refractive indices of the aforementioned components n_1, n_2, and n_3; and the thickness d and electro-optic coefficient r_{33}, both of the $LiTaO_3$ crystal.

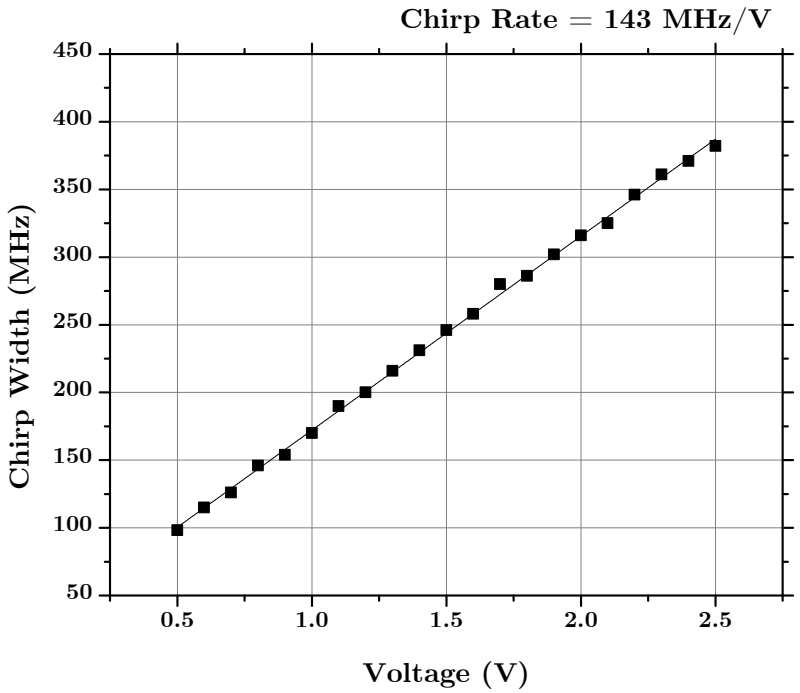

Figure 2.2: Chirp rate of master laser versus voltage applied across the EOM. Chirp rate here is approximately 143 MHz/V, greater than that of past systems [2, 3].

Due to the upper state lifetime being significantly longer than the laser cavity decay time, oscillations in the intensity of the output may occur using just the Nd:YVO_4 laser as it attempts to reach a steady state value of frequency. These relaxation oscillations occur over a significant

timescale compared to the pulse duration (typically 150-200 ns) and are described by the Statz-DeMars equations:

$$\frac{dN}{dt} = \Lambda - \frac{N}{\tau_2} - I \cdot N \cdot \frac{\sigma}{h \cdot \upsilon}, \tag{2.2a}$$

$$\frac{dI}{dt} = c \cdot \sigma \cdot N \cdot I \cdot \frac{l}{L} - \frac{I}{\tau_{cav}}. \tag{2.2b}$$

Variables in the equations include the upper-state population N, the upper-state excitation rate Λ, the upper-state lifetime τ_2, the laser intensity I, the stimulated emission cross-section σ, the length of the active medium l, the length of the cavity L, and the cavity decay lifetime parameter τ_{cav}.

Using an Nd:YVO_4 laser reduces the timescale of the relaxation oscillations compared to an Nd:YAG laser, however a steady state is not reached fast enough compared to the pulse duration. To further reduce the relaxation oscillations, the Nd:YVO_4 master laser is coupled to the *slave*, a second laser diode emitting at approximately 1064 nm. The slave laser emits at the frequency of the master with no effect from the relaxation oscillations.

2.2.2 Initial Amplification and Pulse Shaping

A commercial Ytterbium based fiber amplifier increases the output of the slave laser to 1 Watt while retaining the inputted frequency, as seen in part II of Fig. 2.1. A beamsplitter then separates and polarizes the beam into two arms with each beam passing through a $LiTaO_3$ intensity electro-optic modulator (IEOM) which turns the inputted CW beam into a pulsed beam. The temporal profile of each pulse is determined by the input voltage, which is shaped using a commercially available arbitrary function generator. Pulse durations for the system can range between $10 - 1000$ ns and are controlled with the arbitrary waveform generator. The pulse was approximately 150 ns for the experiments outlined here. A custom made LabView program allows modification of the voltage pulse shape outputted by the function generator, which results in a change in the shape of the optical pulse. IEOMs were chosen because they may be driven with low voltages (< 10 V)

compared to Pockel's cells which require fast switching in the kilovolt range. A disadvantage of this technique however is that the output may drift over time, requiring modifications to the voltage offset and the shape of the arbitrary voltage signal immediately before, and sometimes during, data collection.

To produce the pulses for a single-shot configuration, the arbitrary function generator sends a signal to the first IEOM, opening it creating a pulse. During this time, a constant voltage is applied to the master laser's intracavity EOM leading to a pulse of constant frequency. After an approximately 400 ns delay, the function generator sends the second arbitrarily shaped voltage signal to the second IEOM, opening it to produce a pulse. This signal also triggers a chirped voltage signal to be sent to the master laser's intracavity EOM, creating a frequency chirp in the pulse produced by the IEOM. The first, unchirped pulse passes through an 85 m delay line, syncing it in time to the second pulse.

After these steps a relative frequency difference is present between the two beams as is required for single-shot CRBS. The beams however do not yet have enough energy to generate a lattice structure or a probe beam strong enough to produce a distinguishable signal beam, necessitating further amplification.

2.2.3 Final Pulsed Amplification

Each pulse is amplified from approximately 100 nJ to 400 mJ by one of two identical arms. Each arm is composed of four diode pumped amplifiers (an upgrade from three in previous systems) placed in series as seen in Fig. 2.3.

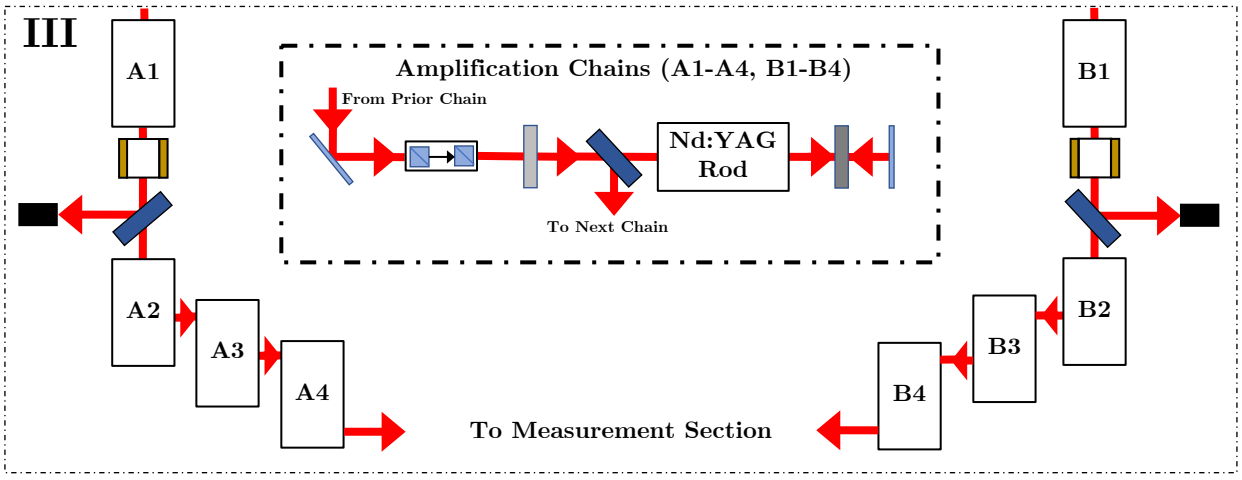

Figure 2.3: Schematic of part III of the CRBS setup showing the four amplification stages for each pump beam. Legend for parts can be found in Fig. 2.1.

The beam goes through each rod in a double pass configuration, as outlined in Fig. 2.4. It first passes through lenses to magnify the beam to 80% of the diameter of the amplifier rod. The beam then passes through a Faraday rotator followed by a half waveplate, thin film polarizer and finally the diode pumped amplifier itself. This ensures the polarization is aligned so the diode outputs the maximum intensity while also preventing feedback to previous amplifier rods. The beam then passes through a quarter waveplate and reflects off a mirror, going through the quarter waveplate and diode pumped amplifier a second time and exits the rod upon reaching the thin film polarizer, now with an orthogonal polarization compared to before. As the beam goes through each of the four diode pumps, the energy is increased from approximately 100 nJ to 400 mJ. Throughout the setup, a series of lenses also progressively increased the diameter of the beam to be 80% the diameter of the next rod, as specified by the manufacturer of the diodes.

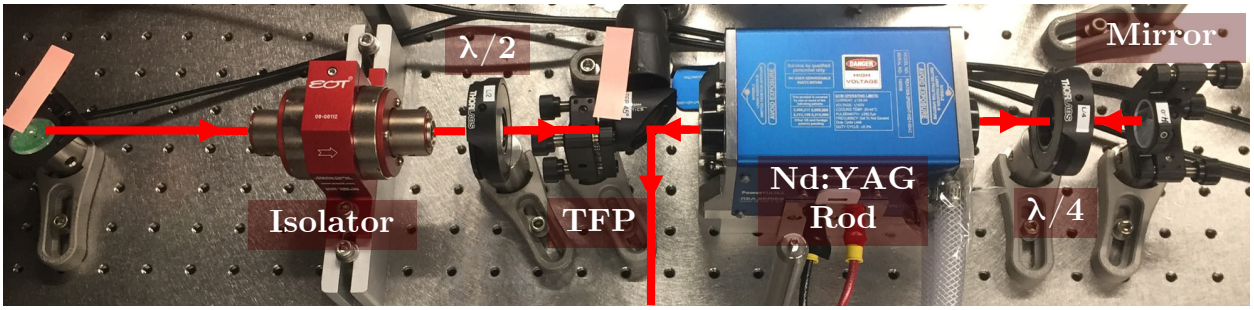

Figure 2.4: A typical rod including (from left to right) a Faraday rotator or isolator, half wave plate, thin film polarizer, diode pumped amplifier, quarter waveplate, and mirror. Beam path through the rod is shown.

To avoid overheating, one chiller is used to cool each arm. Since the amplifiers are diode pumped, the absorption characteristics of the diode must be temperature tuned to match the wavelength of the seed beam for maximum output efficiency. As a result the amplifiers for the chillers are set to a specific temperature to further increase the strength of the signal, as determined in Fig. 2.5.

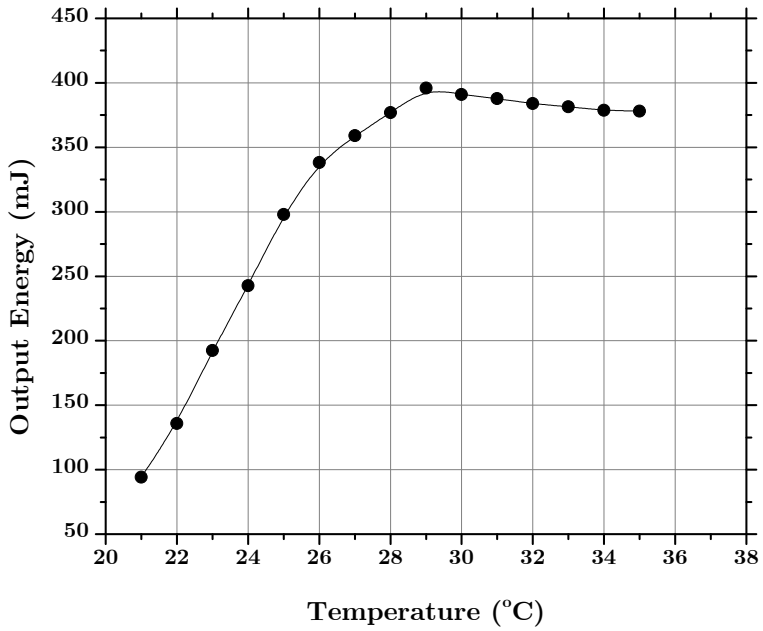

Figure 2.5: Output energy versus chiller temperature for the four amplifier stages composing the left pump beam.

2.2.4 Dual Color CRBS

Previous CRBS systems utilizing pump and probe beams of the same frequency could obtain lineshapes down to approximately $50 - 100$ Torr in air. In order to measure neutrals in partially ionized environments such as low pressure DC glow discharges, which often occur at pressures below this limit, a stronger signal is necessary. Improvements in signal to noise ratio are also desirable for higher pressure and density scenarios in order to obtain better lineshapes.

To allow measurements at lower ambient pressures, the probe beam is frequency doubled to 532 nm while the pump beams remain at 1064 nm. Throughout the rest of this work, using a

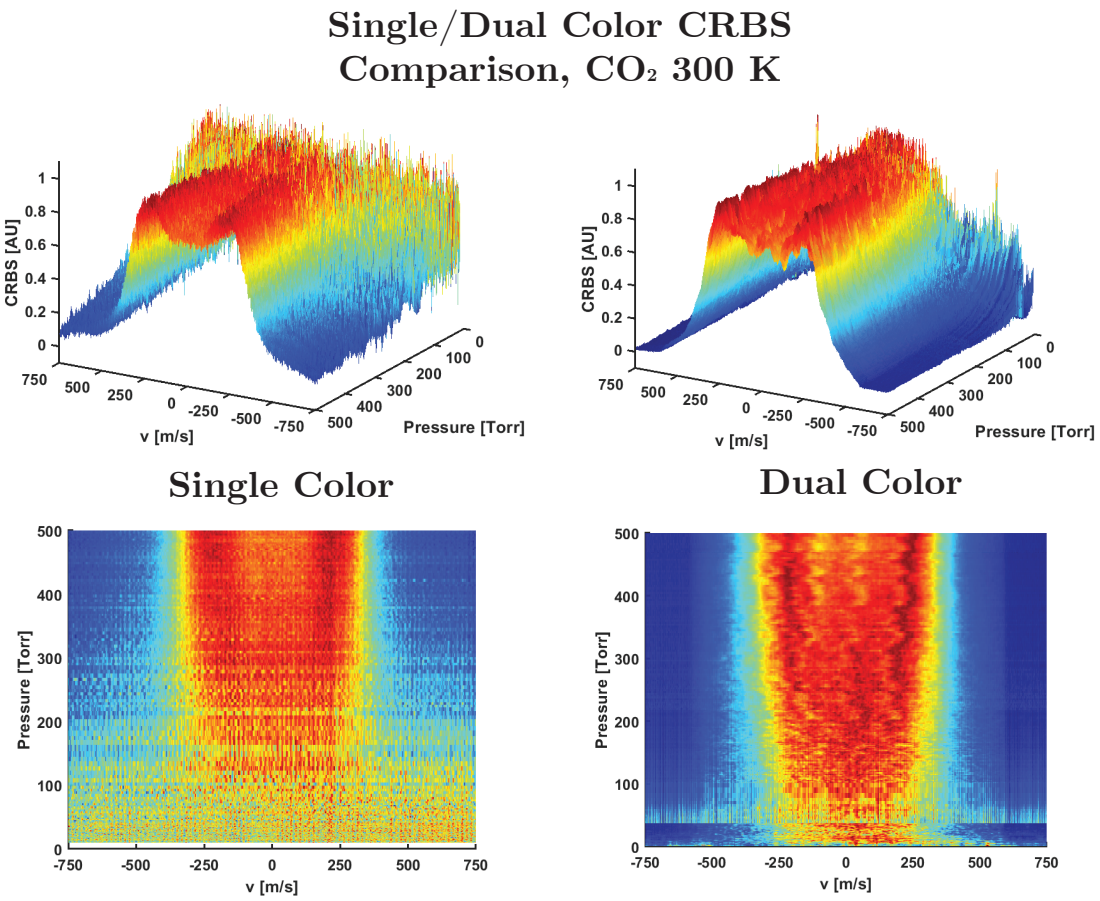

Figure 2.6: Comparison of spectra with a 1064 nm (single color) versus a 532 nm probe (dual color) at various pressures for CO_2 at 300 K.

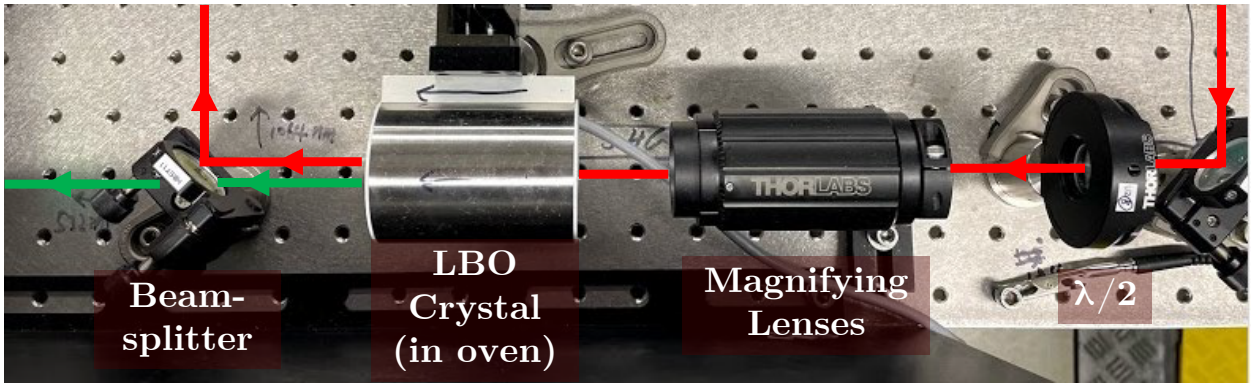

Figure 2.7: Setup used to frequency double the probe beam. The probe is extracted from the pump using a thin film polarizer. The probe then passes through a halfwave plate and magnifying lens to ensure it has the correct diameter and direction of polarization. It then enters the LBO crystal where a portion of the beam is frequency doubled to 532 nm. A harmonic beamsplitter separates the 1064 nm and 532 nm beams, directing the 1064 nm beam towards a beam dump while allowing the 532 nm beam to continue.

532 nm probe beam and 1064 nm pump beams for CRBS will be referred to as the dual color CRBS setup while using the same wavelength for all pump and probe beams will be called the single color setup. As seen in Eqn. 1.6, the strength of the Rayleigh signal is proportional to λ^{-4}. Therefore, the 532 nm probe beam yields a signal sixteen times stronger than the signal produced in previous iterations with a 1064 nm probe. The optical background from the 1064 nm pump beams is spectrally filtered using bandpass filters before the signal reaches the 532 nm detectors, further decreasing the noise present in the lineshape. The setup also implements high-gain photo-detectors designed for 532 nm light, which have better quantum efficiencies than most photo-detectors optimized for 1064 nm. A comparison of spectra derived from the single and dual color setups was conducted in various gases to evaluate the difference in signal resolution. As seen in Fig. 2.6, with a single color setup, or a 1064 nm probe, spectra down to approximately 100 Torr are resolved in carbon dioxide at room temperature as mentioned previously. With the dual color setup or 532 nm probe however, the spectra may be resolved to below 10 Torr.

The probe beam is frequency doubled as recommended by the manufacturer of the diode pumps[2] and is pictured in Fig. 2.7. To obtain the probe beam, first a portion of one of the pump

[2]Northrop-Grumman

beams is obtained using a thin film polarizer. A lithium triborate (LBO) crystal heated to a specific temperature is used to produce the 532 nm beam through second-harmonic generation. Essentially, two photons of equivalent energy combine inside the crystal forming one photon with double the energy, thus doubling the original wavelength due to Eqn. 1.3. Between the thin film polarizer and crystal, the beam passes through a half wave plate and series of lenses to ensure it is the proper diameter and polarization upon entering the crystal. After the crystal, a harmonic beamsplitter separates the 1064 nm portion of the beam from the 532 nm portion, sending the excess 1064 nm portion to a beam dump and preparing the 532 nm portion for four wave mixing by passing it through another half wave plate.

Ensuring the 532 nm beam produced the highest output energy required aligning the beam through the LBO crystal, collimating the beam at the manufacturer's specified diameter, and tuning the crystal to the proper temperature as seen in Fig. 2.8.

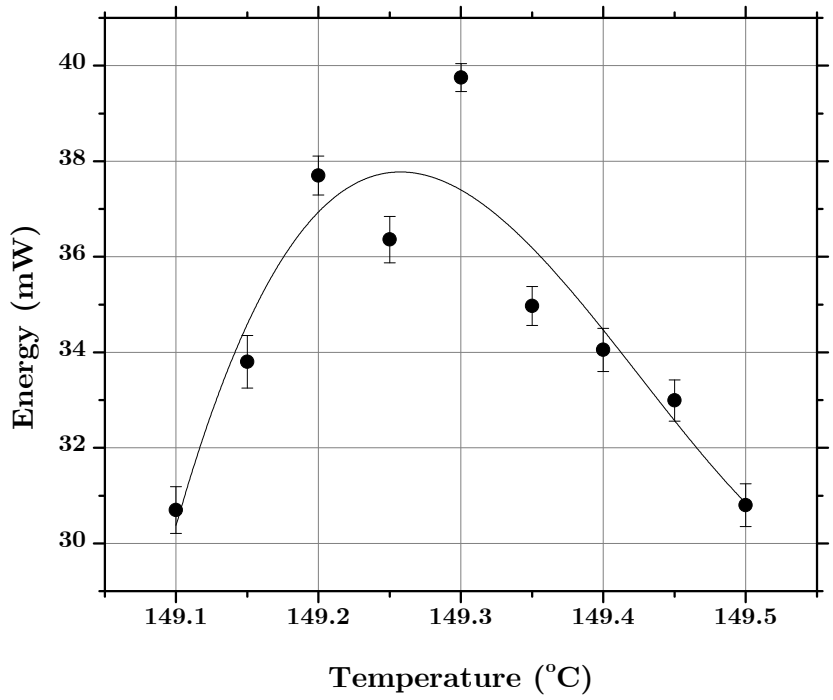

Figure 2.8: Oven temperature versus output energy of 532 nm probe beam.

2.2.5 Alignment of Pump and Probe Beams

In order for CRBS to occur and a signal beam to be generated, the pump and probe beams must be aligned at precise angles to achieve phase matching conditions. With a 532 nm probe and 1064 nm pump beams, the Bragg angle is $\theta = 30°$ according to Eqn. 1.16. Subsequent experiments with vacuum chambers were designed to accommodate this angle. The basic alignment along with frequency doubling of the probe beam are illustrated in Fig. 2.9.

After being produced in the four wave mixing configuration, the final, coherent signal beam then propagates approximately 10 m to reduce the intensity of the background noise, which radiates incoherently proportional to r^{-2} where r is the distance from the measurement location as discussed previously.

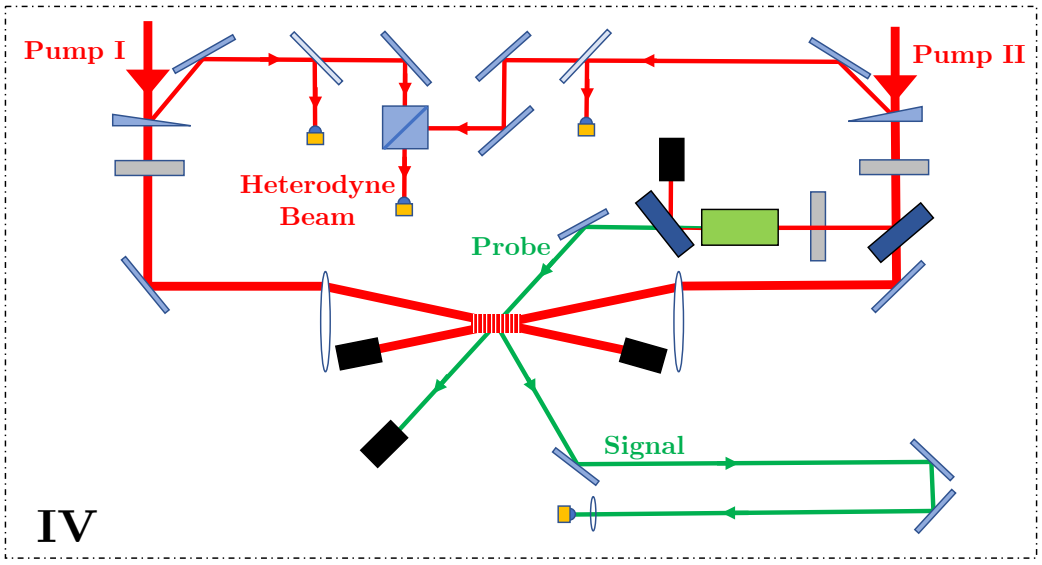

Figure 2.9: Schematic of part IV of the CRBS setup showing the extraction of the probe beam from one of the pumps, frequency doubling of the probe beam, and four wave mixing to produce a signal beam. Legend for parts can be found in Fig. 2.1.

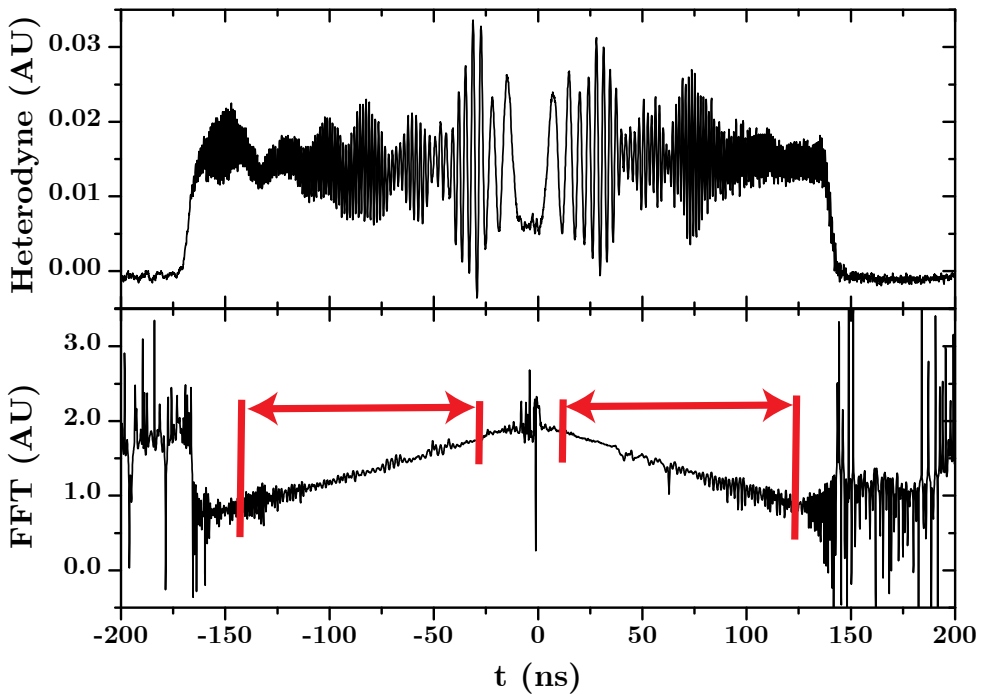

Figure 2.10: Example heterodyne signal (top), or combination of left and right amplified pulses, in the temporal domain. After using a fast Fourier transform algorithm, a change in frequency of the master laser over time can be determined by averaging the slope between the points marked in with red arrows. Noise at the center and ends of the FFT is disregarded.

The frequency of the chirp over the pulse duration is viewed using the method presented by Fee [79]. A portion of each of the two pulses is combined together to form a heterodyned signal and observed using a fast photodiode. The heterodyne signal is subjected to a fast Fourier transform algorithm, which gives a rising and falling slope corresponding to the change in frequency with respect to time, as pictured in Fig. 2.10. From these slopes and their point of intersection, the instantaneous frequency of the beat signal at a point in time can be matched with the CRBS signal at that same point in time, determining the domain of the spectrum.

2.3 Temperature Measurement Results

Temperature measurements were first performed in a variety of gases to evaluate spectra with stronger pump beams and while using the dual color CRBS setup. The study looked at changing temperatures between 300 K and 500 K for xenon, carbon dioxide, and nitrogen gases at multiple

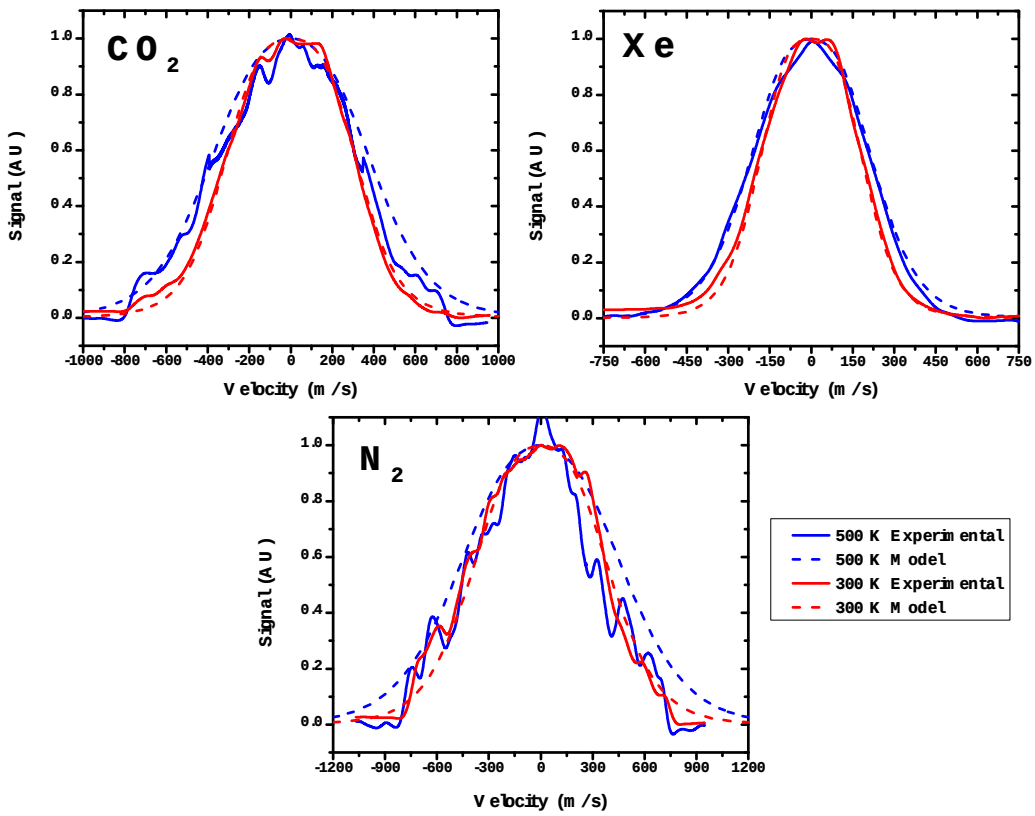

Figure 2.11: Modelled and experimental lineshapes at 100 Torr pressure for temperatures of 300 K versus 500 K for carbon dioxide, xenon and nitrogen.

pressure values to show the relation of the temperature to the width of the spectra, specifically at the full width half maximum. Measurements were performed inside a heated hexagonal box in a vacuum chamber. Two thermocouples measured the temperature of the box, one on the top and one below, and the temperatures averaged. The box was heated first to approximately 500 Torr then measurements were taken at a rate of 10 Hz as it cooled. Pressure was controlled to stay constant while temperature changed. The experimentally obtained lineshape is compared to the s7 model [80] at various temperatures as seen in Fig. 2.11 to evaluate agreement. As expected, xenon produced closest agreement followed by carbon dioxide due to them having the highest polarizability values of the tested gases. Disagreement between the model and experimentally

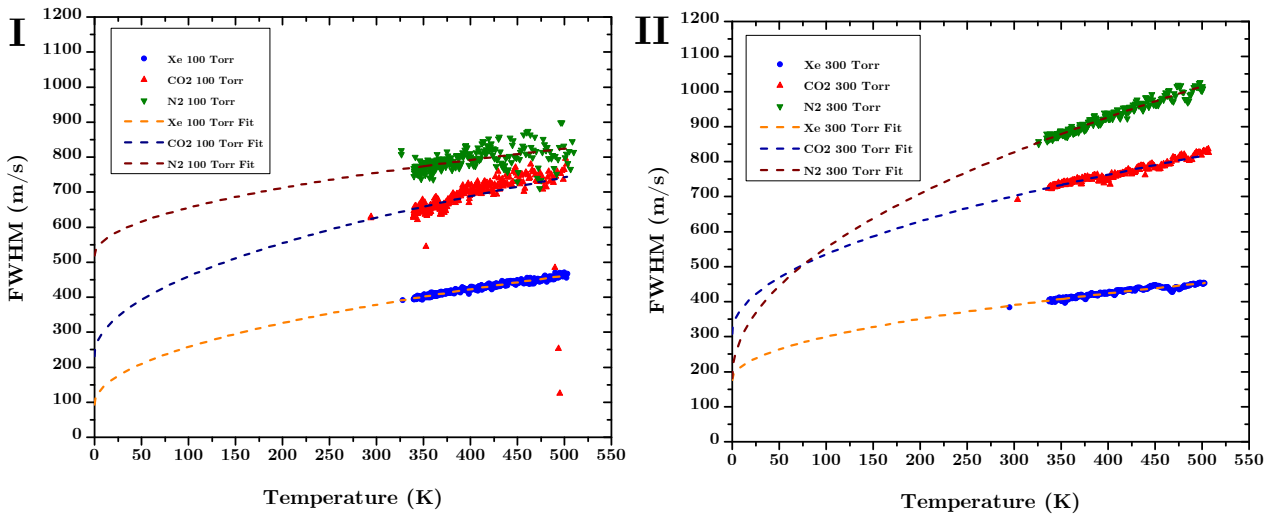

Figure 2.12: Full width half maximum versus temperature for xenon, nitrogen and carbon dioxide at 100 Torr (I) and 300 Torr (II).

obtained spectra may be attributed to optical noise in the system, such as reflections from the probe beam in the chamber. The lineshape widens for all measured gases as temperature increases as predicted with the s7 model.

Although temperature is directly derived by fitting the CRBS spectrum to Eq. 1.19, the full width half maximum value of the lineshape may be determined to help understand the rate at which the spectrum widens. Fig. 2.12 graphs the full width half maximum values of the normalized lineshapes between 300 K and 500 K, approximately the minimum and maximum temperatures under study, at both 100 Torr (left) and 300 Torr (right). Throughout the measurements, pressure within the chamber and thus density were kept approximately the same. These measurements support that the full width half maximum of the spectrum is proportional to the square root of the translational temperature of the gas for low y-parameter values.

2.4 Density Measurement Results

The relation between signal intensity and density was also studied in a gas environment before moving to an environment containing ionized particles. The lineshapes of various gases were recorded as the pressure dropped from atmospheric pressure (760 Torr) to approximately 1 Torr

to assess if the intensity is proportional to the square of the neutral gas density. Spectra were obtained at a rate of 10 Hz with acquisition times approximately 150 ns while the pressure of the chamber was slowly reduced using a vacuum pump. The interior temperature of the chamber was recorded to ensure it remained the same throughout the experiment. Each measurement campaign took between $10 - 15$ minutes to reduce the size of gaps between pressure values for each spectrum. The lineshapes are compared to the s7 model at various pressures, with Fig. 2.13 viewing normalized lineshapes of xenon, carbon dioxide, nitrogen and argon near atmospheric pressure and room temperature. Brillouin peaks, at locations approximately equal to the speed of sound of the medium, are visible in all gas species. Although the s7 model is symmetric in all cases, parts of the

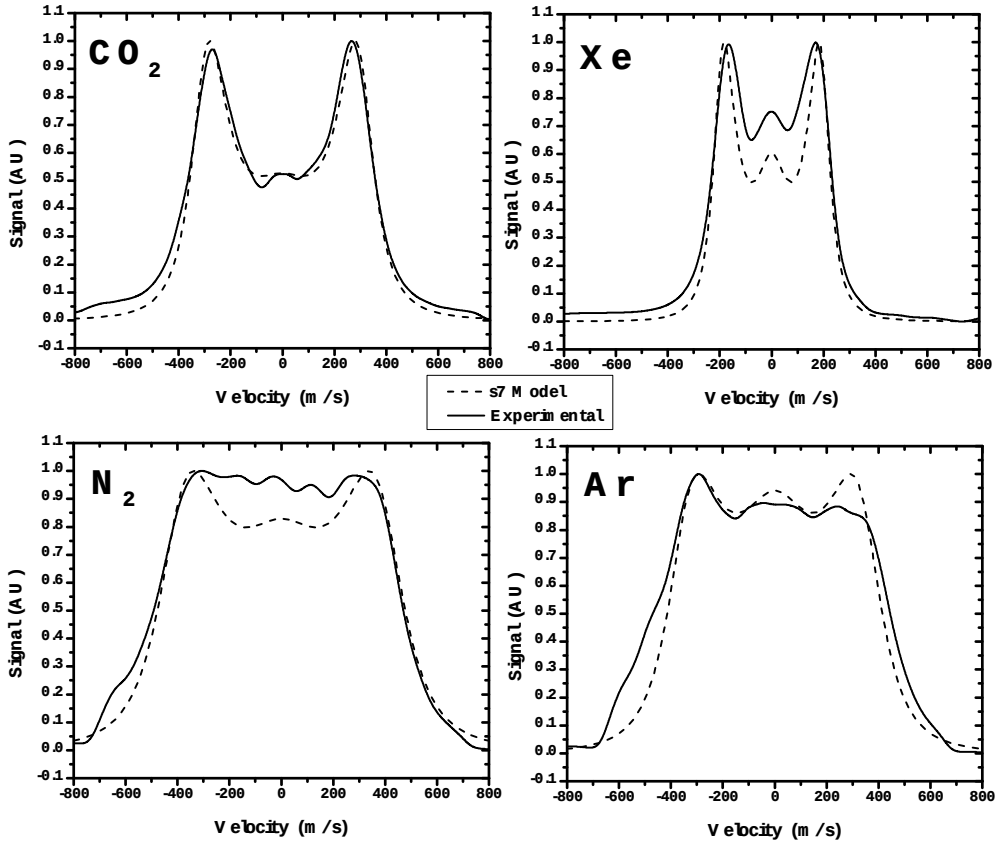

Figure 2.13: Normalized lineshape for xenon, carbon dioxide, nitrogen, and argon at 760 Torr and 300 K.

experimental lineshapes are not. This is particularly noted with argon and is due to an inconsistent intensity in individual pulses in the output of the EOM. As seen, the experimental and modelled lineshapes are generally the same width, with argon showing the most variation.

Determining the neutral density requires measuring the signal intensity first at a known pressure and temperature, allowing determination of the density. Knowing that the density is proportional to the square of the intensity, the values at other unknown pressures or densities can then be determined. To account for a drift in intensity over time due to changing pump energies, the ratio of the total intensity between the sum of the intensities of the pump beams and the signal intensity is measured.

Intensity values are plotted in relation to pressure of various gas species in Fig. 2.14. The exact intensity values measured are arbitrary and depend on the strength of the signal beam, which itself is based on a variety of factors including beam alignment, total energy of the pump and probe beams, and alignment of the signal with the photomultiplier tube. It may not always be assumed between measurement campaigns that the intensity will remain the same at an equivalent gas temperature and density, especially if a long period of time has passed between campaigns.

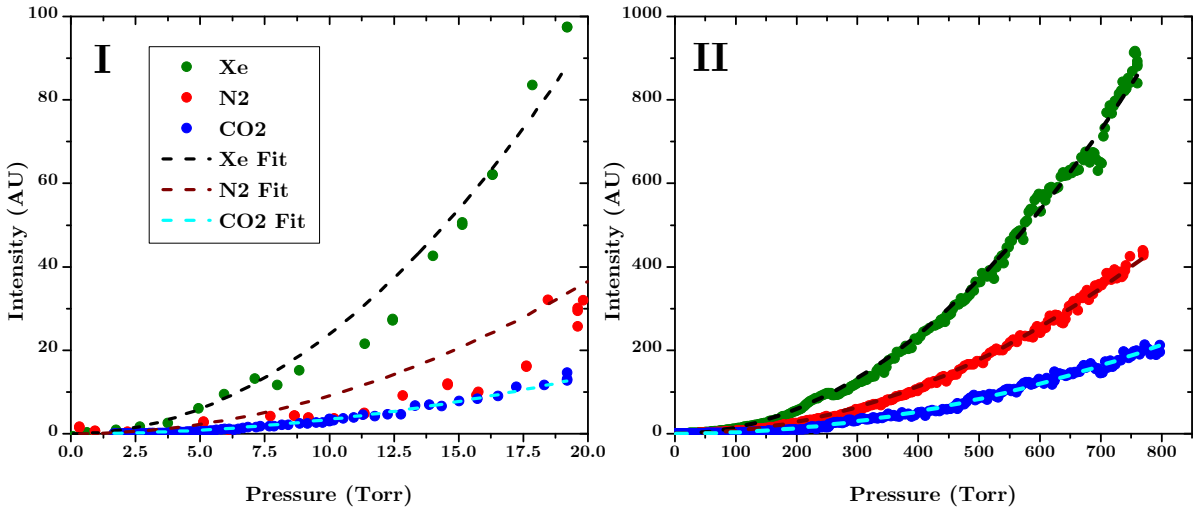

Figure 2.14: Normalized intensity versus pressure for xenon, nitrogen and carbon dioxide at low (I) and high (II) pressures.

As seen in Fig. 2.14, xenon has a higher intensity than nitrogen due to its higher polarizability. Carbon dioxide is expected to have an intensity between that of nitrogen and xenon, however it does not due to data collection occurring on a different day. As seen in part I of the figure, the relation between density and intensity generally continues to hold at lower pressures, particularly for xenon. The intensity of the photomultiplier tube was increased at lower pressures, leading to higher intensity values depicted in part I of the figure compared to part II. This was done to better see the lineshapes at lower pressures. Data becomes noisier at these low values due to a smaller signal to noise ratio.

3. MEASUREMENTS IN A GLOW DISCHARGE

As outlined in Sect. 1.1, this work measures neutral density and translational temperature in a partially ionized environment by using single-shot CRBS. A glow discharge is used to produce the ionized environment due to its low ionization ratio. First a background on electrical discharges is described. Then an outline of the chamber and electrical schematic used to produce the glow is presented, and finally density and temperature measurements of the glow are given.

3.1 Background on Electrical Discharges

Often called the fourth state of matter, plasmas occur as some of the particles in a gas ionize, leaving approximately equal numbers of positively charged particles (ions) and negatively charged particles (electrons). The ionization ratio (α) gives the ratio of ionized to neutral particles in the plasma [81]. While plasmas can be tens of thousands of degrees in some environments such as in stars, low-temperature or cold plasmas (those with temperatures less than 1000 K) may also occur and are often used in laboratory settings [82, 83, 67]. Electrical discharges may be used to produce plasma by creating a voltage difference between two conductive surfaces known as the anode and cathode. To demonstrate CRBS measurements in an ionized environment, this work uses an electrical discharge, more specifically a glow, in order to measure properties of neutral particles more easily due to the low ionization ratio. The relative ease to set up and the use of lower, and thus safer, currents and temperatures are also advantageous when conducting the experiments.

Several types of electrical discharges may occur depending on the ionization ratio of the particles in the gas, notably the dark, glow and arc discharges. The ionization is largely dependent on the magnitude of the current, however other factors including the pressure and species of gas and the size and material of the electrodes dictates the threshold values for current and ionization ratios between the types of discharge. The main classes and subcategories of each discharge type are explained here.

3.1.1 Dark Discharges

If an electrical discharge does not have enough current for a glow, it is considered to be in the dark discharge regime. The dark discharge is named because the ionization is not visible to the human eye. At extremely low currents (on the order of 10^{-10} A), background ionization occurs [84]. The weak electric field pushes ions and electrons naturally present from background radiation to the electrodes. Eventually the saturation region is reached when all background ions and electrons have reached the electrodes. In this region, which occurs with current on the range of 10^{-9} A, the current remains constant as voltage is increased.

The Townsend discharge occurs just below the breakdown voltage as current rises exponentially with voltage [85]. In this regime the electrons acquire enough energy to ionize a neutral atom as they travel in the electric field to the anode. The electron emitted from the neutral particle has enough energy to ionize another neutral particle creating an avalanche effect. This discharge is typically not visible until it approaches the breakdown voltage and transitions to a glow. Corona discharges that form in this regime near sharp edges of the anode or cathode may be visible however.

As the voltage applied across the electrons increases, electrical breakdown eventually occurs when ions and photons impact the cathode releasing electrons, meaning the ionization is sustained. Enough photons are released so the discharge becomes visible to the human eye. Current continues to increase while the voltage drops to the breakdown voltage, where it will remain nearly constant while in the glow regime.

3.1.2 Glow Discharges

Glow discharges are of primary interest in this study because they produce more noticeable changes in neutral density and temperature compared to dark discharges.

For a normal glow discharge, the area of the electrode covered by the glow is proportional to the current, however the voltage between the electrodes remains nearly constant because it is independent from the current [84, 83]. Experiments presented in this chapter are typically in the

normal glow discharge regime.

As the current increases and the entire cathode surface becomes involved in the discharge, an abnormal glow is reached. Here the voltage gradually begins to increase with further increases in current [8].

Eventually as more current is applied to the abnormal glow, an abrupt transition characterized by a sudden increase then sharp decrease in voltage occurs as the arc discharge regime is entered. This regime sees a high current density and a voltage that drops with increasing current. The arc begins in the non-thermal regime where the ionic temperature is less than the electron temperature. The thermal regime is reached when the ionic temperature and electron temperature are approximately equal, leading to little voltage change with applied current.

3.1.3 Anatomy of a Glow Discharge

Several different regions may be defined within a glow discharge. The exact proportions of each region, and whether a region is even present, depends on a number of factors including the pressure, electrode spacing, current, and the size of the chamber housing the discharge region [86]. The two main sections are the cathode glow and anode glow. Subsections of these regions are pictured in Fig. 3.1 and are described below moving from the cathode to the anode.

The cathode itself is composed of an electrically conductive material, such as copper used in this study. As ions contact the cathode surface, electrons are emitted from the cathode and begin their journey across the discharge region. The Aston dark space occurs immediately after the cathode. Here electrons possess an energy too low for neutral particles to become ionized, resulting in a dark layer. Occurring next is the cathode glow, where electrons gain enough energy and accelerate to a high velocity. As the electrons collide with neutral atoms, the atoms are excited into higher energy levels. As the atoms relax and return to lower states, they emit photons producing visible light, the frequency proportional to the energy difference between the excited and ground states.

Afterwards the particles enter the cathode, or Crooke's, dark space. Here exists the largest voltage drop in the discharge, as atoms are ionized and accelerate towards the cathode. Because

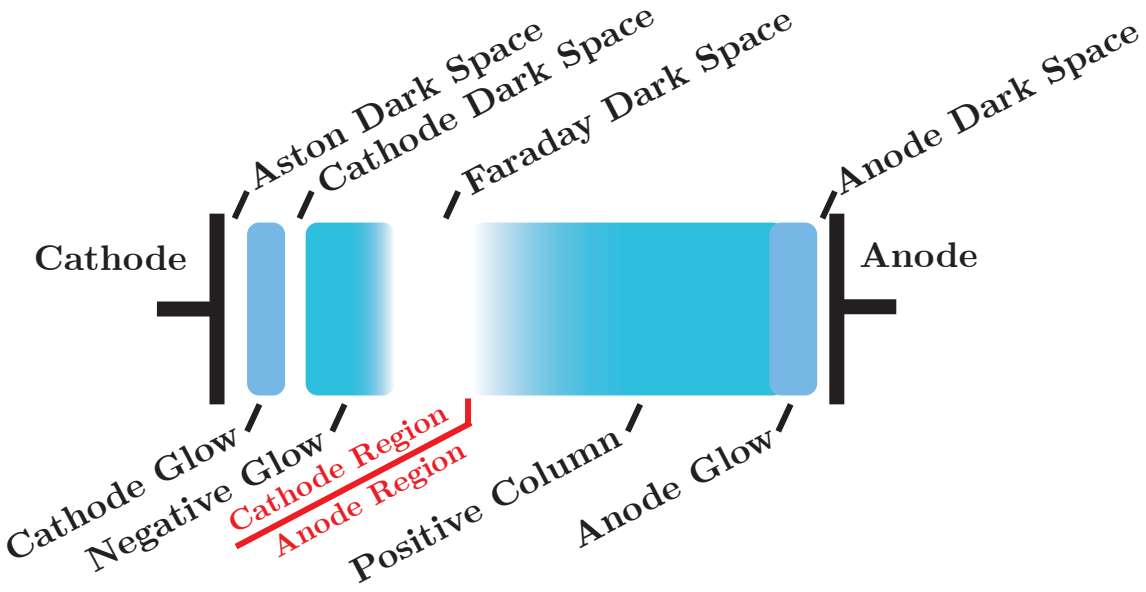

Figure 3.1: Components of a typical glow discharge.

the atoms are ionized as opposed to excited to higher energy levels, little to no light is produced in this region. This region is larger for lower pressures since the mean free path is higher. As the electrons progress, they slow down and recombine with ions through Bremsstrahlung radiation [87], beginning the negative glow region. This typically produces the highest light intensity of the glow. As electrons continue losing energy, they no longer have enough energy to ionize or excite atoms, so less light is produced. This is known as the Faraday dark space. This region does not always appear, particularly for higher pressures or small electrode spacings. The Faraday dark space is the last component of the cathode glow.

After the Faraday dark space comes the positive column. This is typically the largest section of the glow, with properties uniform longitudinally along the axis and symmetric radially. Here electrons have high energies ionizing and exciting atoms, leading to a consistent glow. Ion and electron densities are approximately $10^{15} - 10^{16}$ m^{-3} [81]. This region typically sees the largest extension or contraction when the distance between the electrodes changes. Next is the anode glow. This region sees an increase in the electric field, thus higher electron energies and a release

of photons, as particles are raised to an excited state then relax again. Finally, immediately before the anode is the anode dark space, where fewer electrons are present and no visible light is emitted.

3.2 Design

Before beginning measurements, a chamber was built in order to house the glow discharge. The chamber was built to be larger than previous, similar designs [88, 89] to be able to run a glow discharge and possibly other future experiments including an arc for as long as possible without overheating. The chamber also had to accommodate windows for the pump, probe and signal beams while still allowing easy physical access to the interior of the chamber. Because moving the measurement location by realigning the beams of a four wave mixing technique may be time consuming and cumbersome, the chamber needed to be capable of precisely adjusting its horizontal position. Finally, the chamber needed to be capable of holding pressures near 10-15 Torr for multiple hours without leaking. The design of the chamber and how it satisfies these requirements is described in the subsequent sections.

3.2.1 Main Chamber Design

A vacuum chamber houses the glow discharges and controls the gas type and pressure near the electrodes. The chamber consists of a modified six way cross with 10 inch CF flanges and a 10 inch diameter spherical center. The large size of the chamber is used to avoid overheating of the chamber or medium inside. The geometry of the beams for the dual color setup requires a minimum of five windows in specific locations to allow passage of the two pump beams, the probe and the signal beam through the chamber. The 6 way cross and connecting flanges were modified to create space for 6 windows to allow the probe and signal beam to either enter or exit the chamber at a 60° angle relative to the pumps, as depicted in Fig. 3.2. As discussed in Sect. 2.2.5, this angle is required to satisfy the Bragg equation. Additional nipple flanges may also be added between the windows and chamber to distance the windows from the center, which will prevent debris from ablation depositing onto the windows during future arc discharge experiments.

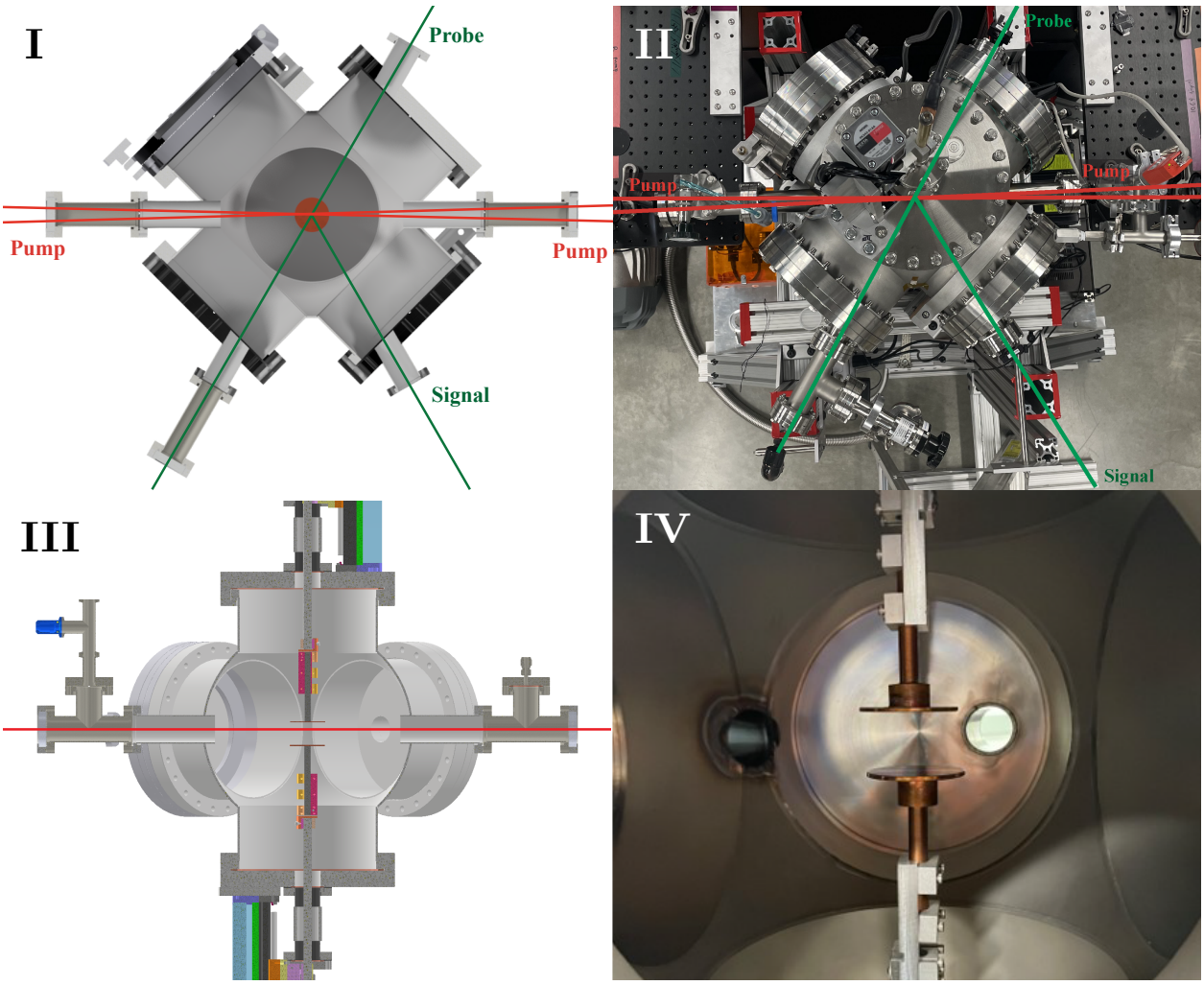

Figure 3.2: Comparison of modelled top view (I) to completed chamber design (II). Overlaid in red are the pump beams moving horizontally, in green the probe beam propagating from the top right to the bottom left, and the signal beam also in green originating in the center and propagating to the bottom left. The bottom of the figure depicts a comparison of a model of the side cutout (III) to the actual chamber interior (IV).

Once assembled in its final configuration, the chamber was leak tested by vacuum pumping the chamber for 45 minutes then allowing the chamber to sit overnight while monitoring the pressure. Results are plotted in Fig. 3.3. This method found a leak rate of approximately $3.8 \cdot 10^{-5}$ L·mBar/s, which is adequate to ensure minimal contamination from surrounding gases when operating at pressures near 15 Torr for multiple hours.

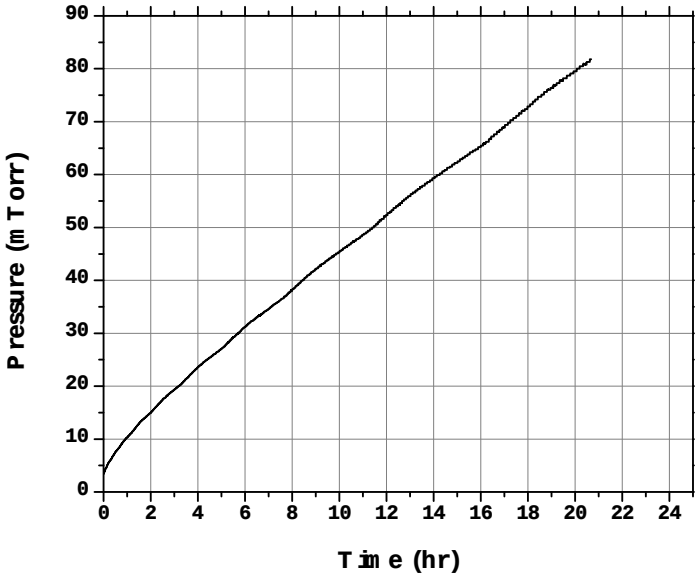

Figure 3.3: Leak rate of vacuum chamber in experimental configuration after outgassing.

In order to move to precise positions along the radius of the glow discharge, two high precision load slides[1] were installed on the bottom of the chamber, one on each leg as depicted in Fig. 3.4. Linear bearings further supported the chamber allowing adjustments in one dimension. The slider was designed to move with a precision of $1/32$ inch, or 0.8 mm. Rulers were placed on each side of the chamber base to ensure each side moved the same distance without rotating the chamber. Wheels were used for rough alignment in both axes on the ground before the sliders secured the stand in position.

Moving the chamber horizontally during data collection presents the possibility of the pump and probe beams becoming misaligned due to changes in the window orientation or a beam clipping the edge of the chamber, potentially reducing the intensity of the signal. Lineshapes were obtained at various horizontal positions in xenon at 15 Torr and room temperature, the starting parameters for most glow discharge experiments, to ensure minimal change in signal due to movements of the chamber. A change in intensity of approximately 10-15% was observed as the slider

[1] McMaster 9222T21

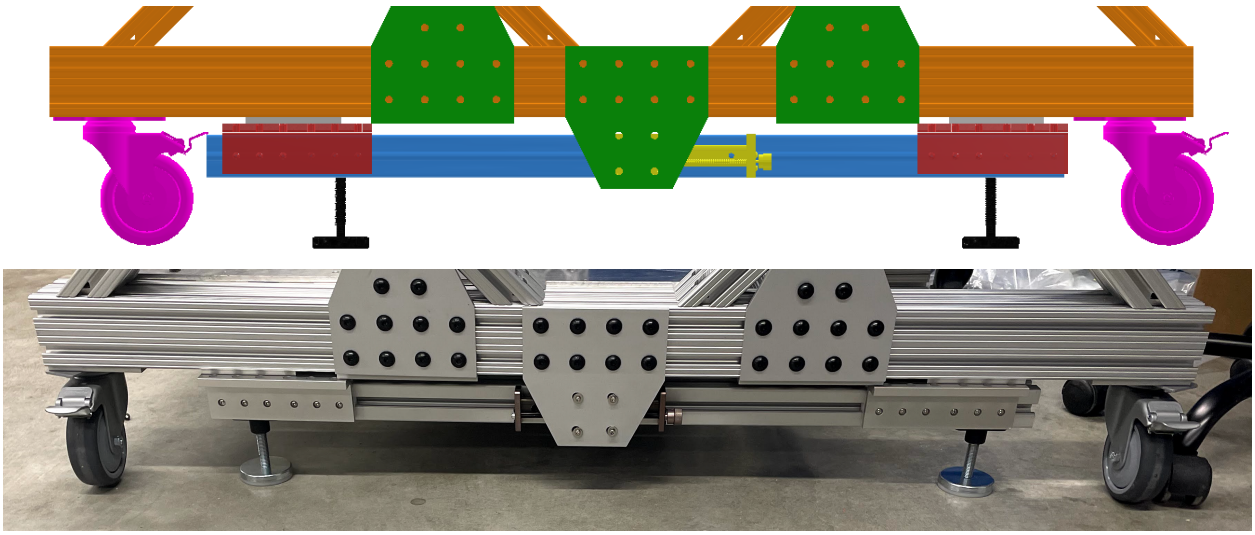

Figure 3.4: Modelled and actual views of translational slider. The blue frame remains stationary on the ground while two sliders (red) move the rest of the chamber laterally.

was moved between minimum and maximum values as seen in Fig. 3.5. This variation was taken into account when evaluating the intensity at different points along the glow discharge.

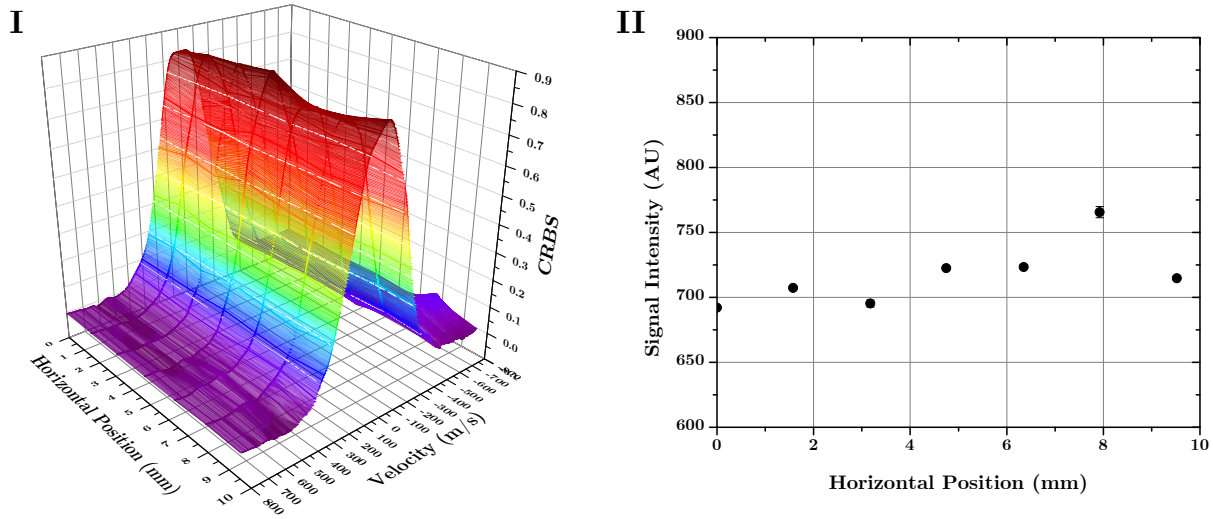

Figure 3.5: (I) Three dimensional plot of CRBS lineshapes in xenon at 15 Torr at various horizontal positions within chamber. (II) The ratio in intensity between the measured signal and the summation of the heterodyne signal is depicted to account for changes in pump beam intensity when the position of the chamber changes.

The distance between electrodes changed using vertical positioners,[2] which had a precision of 0.003 inches or 0.076 mm and a range of 6 inches (152.4 mm) each. The electrodes attached to brass rods which fed through coupling flanges,[3] and connected to the rest of the circuit. The top rod was grounded while the bottom connected to the DC power supply. In order to avoid the current discharging into the chamber, a custom mount made of MACOR attached the brass rod to the axial positioner. Screws made of PEEK further kept the rods insulated. In addition, PEEK pipes surrounded the brass rod at the bottom of the chamber, where a large voltage differential was present, to avoid a discharge forming between the rod and chamber. A custom made plexiglass box surrounded the bottom brass rods where it protruded from the chamber to avoid accidental contact with the circuit.

3.2.2 Electrical Schematic

A glow discharge was chosen due to its stability, with low pressures used to produce a wider radius. The glow discharge uses an electrical circuit consisting of a power supply, ballast resistor, electrodes and a ground wired in series as depicted in Fig. 3.6. The power supply[4] typically produces up to 10 kV and 0-40 mA to produce a glow. The electrodes are copper with a flat, circular head approximately 2 inches (50.8 mm) in diameter. A 10 kΩ ballast resistor is used to limit the current flowing through the circuit and prevent sudden fluctuations. To measure current, a shunt resistor of 195 Ω is located between the cathode and ground with the voltage measured by an NI-DAQ. A high voltage probe with a dividing factor of 1000 is connected to the NI-DAQ to measure the voltage between the anode and ground. The current output per applied voltage was measured during each trial, with part II of Fig. 3.6 showing a sample of current in relation to voltage with xenon at 15 Torr. A positive dependency of voltage related to current above approximately 16 mA suggests an abnormal glow in this region. At approximately 15-16 mA, there is no change between voltage and current, suggesting a normal glow. Also of note is a higher voltage when current is increasing, particularly at lower current values.

[2] Velmex XSlide XN10
[3] Lesker F0275XVC050
[4] Electron Vision Series 105 High Voltage Power Supply

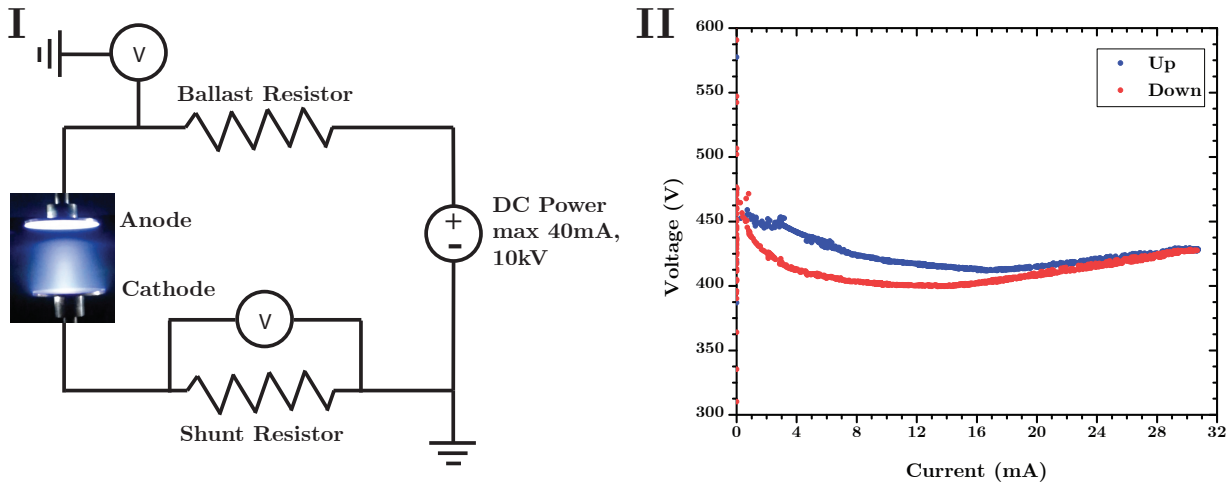

Figure 3.6: Part I shows the electrical schematic for the glow discharge configuration. The ballast resistor is approximately 100 kΩ. Part II depicts the voltage between the anode and cathode versus the current applied for both rising and falling currents for a 15 Torr xenon glow.

In addition to design of the chamber, mirrors and lenses were added to the CRBS laser system to redirect the beams so the four-wave mixing occurs inside the chamber. Two 12x18 inch extensions were added to the optical table so equipment could be placed on either side of the chamber. Lenses with a focal length of 412 mm focus the 1064 nm beams while a 300 mm focal length lens focuses the 532 nm probe beam. These focal lengths were chosen based on the optical table and chamber sizes.

3.3 Temperature and Density Results

In order to demonstrate point measurements with CRBS in the glow discharge, measurements were collected radially from the center to edge of the chamber. This allows viewing of the change in spectra as the properties of the glow change along the radius. Measurements are also collected at various currents to view the change in spectra.

Data is acquired in a glow discharge using the same technique as with pure gases. A typical experimental trial began first by filling the chamber with CO_2 at atmospheric pressure to obtain a signal with well defined Brillouin peaks. From here the offsets and voltage profile applied to the EOMs could be tuned to produce a shape with equally sized Brillouin peaks. The location of

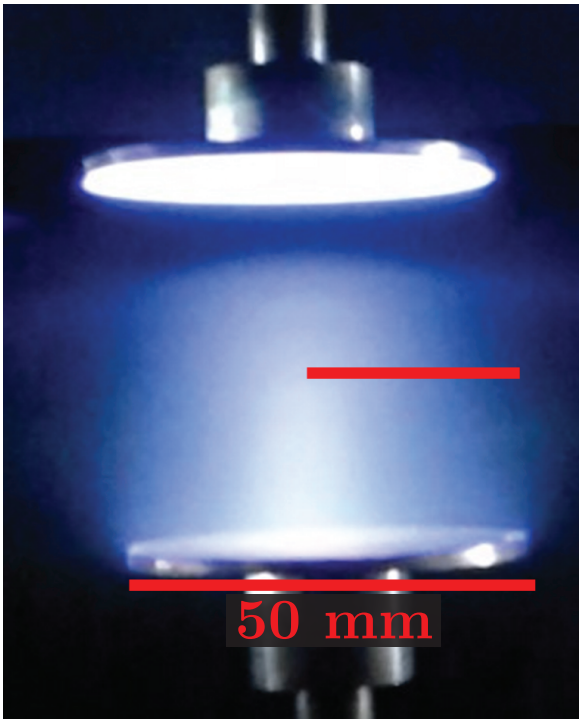

Figure 3.7: Typical glow discharge from 50 mm diameter electrodes. Measurement region from center to edge shown in red.

the peaks in the velocity domain may also be checked to ensure they align with the theoretical speed of sound in the medium. Slight adjustments to the four wave mixing alignment at this step also help maximize the beam signal. The system then remains running as the pressure in the chamber decreases, purging the CO_2 from the chamber and connecting feeder lines. Xenon then enters the system and is stabilized at 15 Torr or another desired pressure. Initial lineshapes are recorded before the discharge is turned on to view the beamshape at a known pressure and temperature (15 Torr at room temperature for example). For these experiments, the oscilloscope typically averaged the previous 20 shots, meaning each saved profile is an average of 20 lineshapes or the previous 2 seconds (assuming chirping at a rate of 10 Hz). The average was increased to obtain a cleaner lineshape if lower pressures or higher temperatures were expected. Finding the temperature and density throughout the glow discharge was done by fitting the lineshape to the theoretical Rayleigh peak equation (Eqn. 1.19) and then comparing the intensity of the current lineshape with the original lineshapes recorded with no glow.

The study measured a glow discharge at a pressure of 15 Torr with electrode separation of 23 mm, which was chosen after testing among several configurations after finding it to produce the most stable glow in xenon. A typical glow in this configuration is seen in Fig. 3.7. The laser was aligned to be halfway between the top and bottom electrodes in the positive column. This region was chosen because it takes up the largest component of the glow. In addition, properties including the ion and electron densities are longitudinally independent and axially symmetric, changing only as distance along the radius is increased.

First measurements were conducted at various currents between 0-25 mA. Applied current slowly decreased over a period of approximately 10-15 minutes while spectra were captured at a rate of 10 Hz as mentioned previously. Increasing current was also tested however the location of the glow on the electrode was found to be less stable, particularly at low current values (below 7 mA). Due to the size of the chamber and the low temperatures associated with the glow discharge, no observable change in temperature or density was detected due to the length of time the current ran for, assuming the applied current and measurement location within the glow remained the

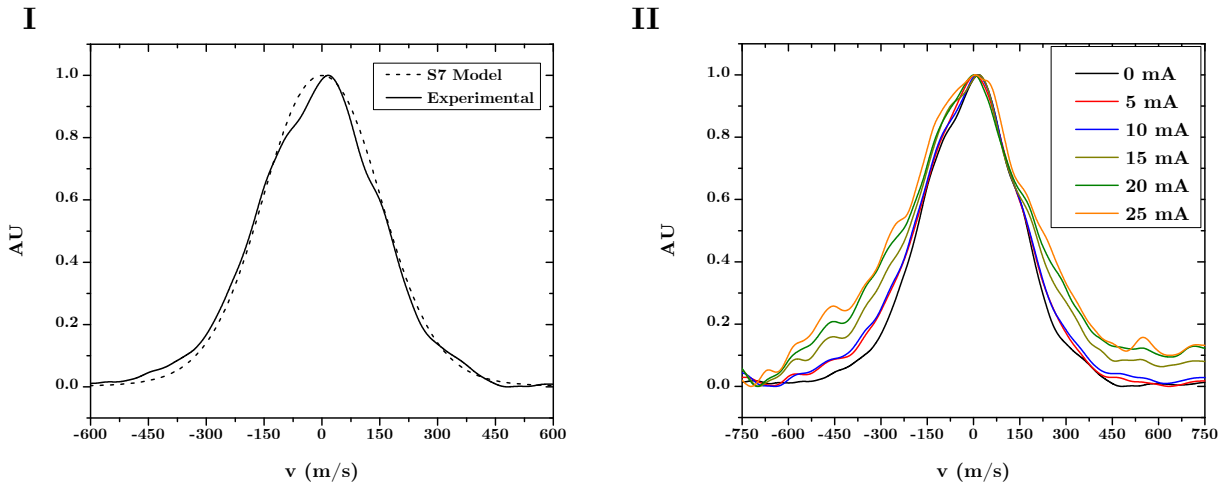

Figure 3.8: (I) Modelled and experimental lineshapes for xenon at 15 Torr with no current applied. (II) Normalized experimental lineshapes for xenon at 15 Torr between 0 mA and 25 mA applied current. A widening in the lineshapes due to an increase in translational temperature of neutral particles is present.

same. Lineshapes remained in agreement with the s7 model, as seen in part I of Fig. 3.8, which depicts the lineshape before current is applied at 15 Torr and room temperature. As more current is applied (part II of Fig. 3.8), the lineshapes broaden as expected.

In addition to widening of the beam profile, an increase in current led to a drop in signal intensity. This may be seen when spectra are plotted in relation to current, as depicted in Fig. 3.9. The intensity at various currents may be compared to the original intensity at 0 mA, taken immediately before starting the glow and after the glow is turned off.

Next measurements along the radius of the glow were collected. A total of nine measurement trials were conducted in a xenon glow discharge at 15 Torr pressure. Approximately 100 samples

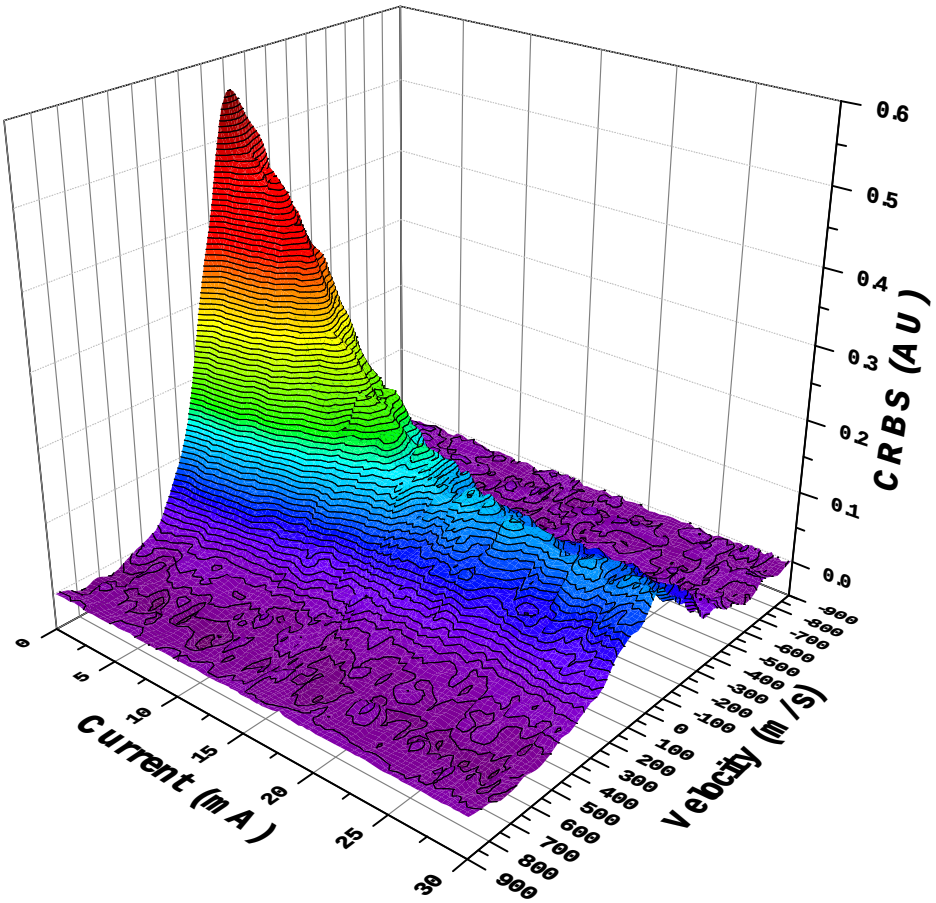

Figure 3.9: Three dimensional plot of CRBS lineshapes in xenon at 15 Torr when subjected to glow discharges of between 0 and 30 mA applied current.

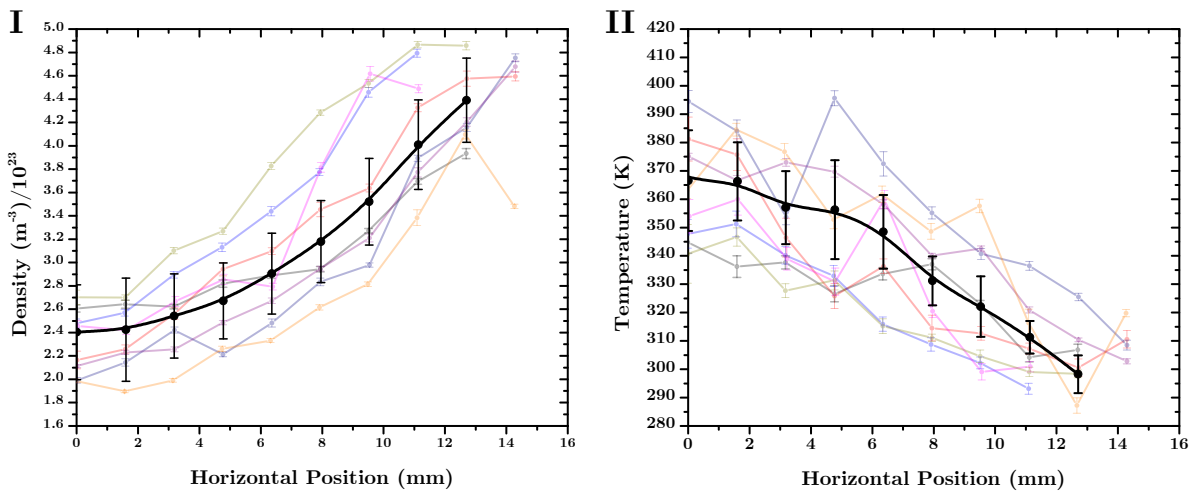

Figure 3.10: Neutral density and translational temperature measured along the radial profiles of xenon glow discharges.

were collected at each radial position within the discharge for each trial. Like the gas and variable current measurements, data was collected at a rate of 10 Hz with a 150 ns acquisition time for each spectrum. Each trial measured at the same locations along the glow, with 2.4 mm or 3/32 in between each measurement location. Measurements from each point were then averaged together with measurements from the corresponding points in the other trials. The 95% confidence intervals in temperature and density were small between lineshapes during the same trial (about 5 K for temperature and $4 \cdot 10^{21}$ m^{-3} for density). However, values obtained between different days were found to vary by nearly 50 K and $6 \cdot 10^{22}$ m^{-3} for temperature and density, respectively. This is attributed to changes in the glow discharge between trials, as the discharge was turned off and on between runs, which occurred on multiple days. Fig. 3.10 depicts the measured changes in translational temperature (part I) and neutral density (part II). Average values are displayed prominently while silhouettes of individual trials are seen in the background.

All campaigns show a general trend of density increasing and temperature decreasing as the measurement location moves from the center to edge of the discharge. The average density at the center of the glow was found to be about $2.4 \cdot 10^{24}$ m^{-3} while the temperature was about 367 K. The average density and temperature at the edges were measured to be $4.4 \cdot 10^{24}$ m^{-3} and 300 K

respectively. Ambient density in the chamber was approximately $4.8 \cdot 10^{24}$ m^{-3} and temperature was 295 K. The average gradients of both density and temperature were found to be smaller closer to the center when compared to the edge. These general trends are seen in glow discharges with other gases in past literature. For instance, in SF_6 in sub-Torr pressures, Ogle [83] found the temperature at the edge of a glow to be 310 K and the center to be 342 K. Measurements here were taken with a thermocouple and had approximately 10% uncertainty. Using filtered Rayleigh scattering, Yalin [67] measured the temperature in the center of an argon glow discharge of 50 Torr pressure to be 400 K with an uncertainty of 40 K. The applied current corresponding to the given temperature was 15 mA in both works. Although these works use different gases and different ambient pressures than the setup used here, they show the general range of temperature values expected for a glow discharge of 15 mA. Overall, these measurements show single-shot CRBS is capable of measuring changes in neutral density and translational temperature in a partially ionized environment.

4. SUMMARY

This work presents an overview of the history and types of optical scattering with an emphasis on Rayleigh and Brillouin scattering, followed by a introduction to various laser diagnostic methods including CRBS. An overview of the dual color single-shot CRBS setup used in this work is presented along with demonstrations of the effects of temperature on the full width half maximum of the CRBS signal's spectral lineshape and of pressure or density on the intensity of the lineshape. Finally the work details the design and use of a glow discharge chamber to simultaneously measure neutral density and temperature at various points radially within the glow discharge and at various applied currents. A decrease in neutral density and increase in translational temperature is seen closer to the center of the glow as predicted.

4.1 Further Study

This work has shown that CRBS measurements of the properties of neutrals are feasible in partially ionized environments. Successful demonstration in a glow discharge shows CRBS may be applied to other partially ionized environments such as a Hall thruster, allowing measurements in regions where diagnostics were previously unobtainable. Analysis of other plasma environments, particularly ones using other gases such as argon or with higher ionization ratios are of interest for further study. However, as polarizability or density decreases and temperature increases, the intensity is reduced requiring higher signal to noise ratios. As seen in Fig. 4.1, although a signal is seen in argon both with and without an applied current, a high amount of noise in the sample could produce large errors in fitting the beam to the Rayleigh lineshape to find temperature. To further increase the signal to noise ratio, more powerful pump beams may be implemented.

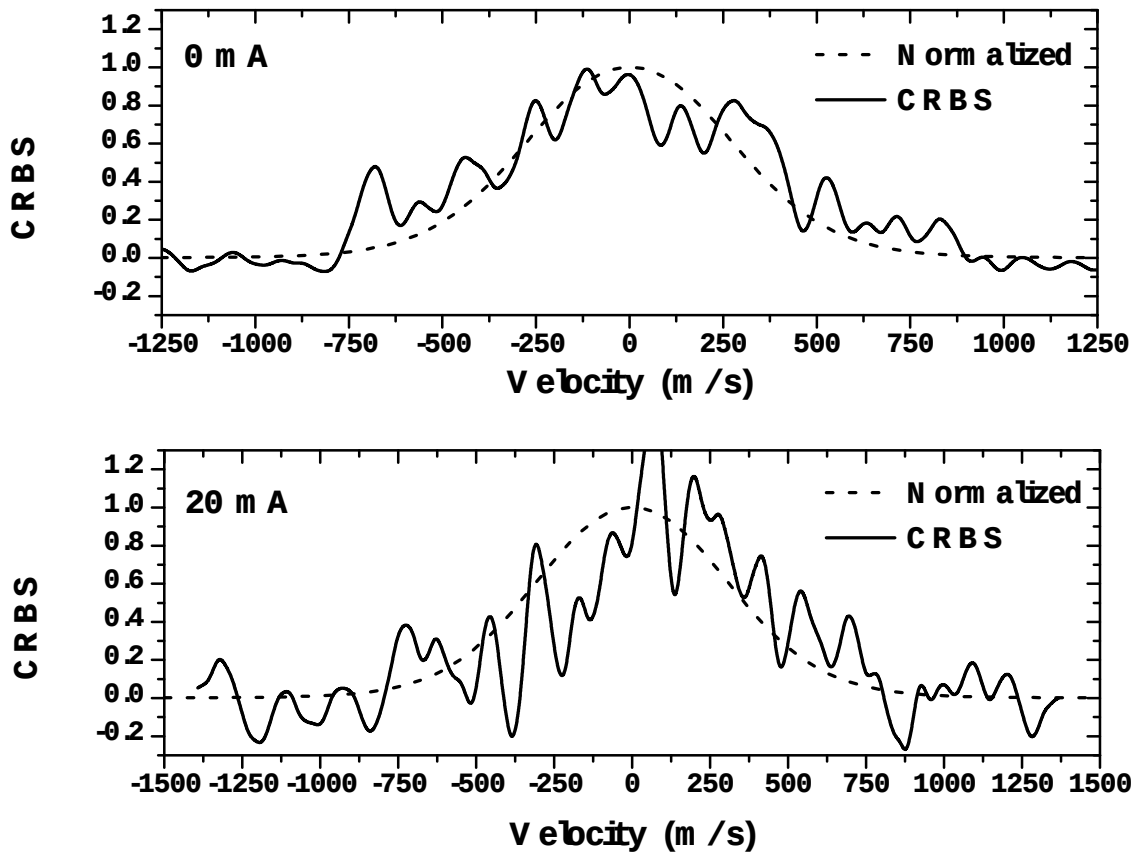

Figure 4.1: Argon lineshape at 15 Torr at room temperature and with 15 mA glow applied.

4.1.1 Arc Discharge

The high density of ions present during the arc discharge as well as the higher pressures of the surrounding neutral gas (in the range of hundreds of Torr) makes conducting CRBS measurements in this regime of interest in the near future. Demonstration of CRBS in an arc discharge may provide insight to the performance of CRBS in other plasma environments with higher ionization ratios such as in a flame or combustion chamber. The chamber designed in this work is well suited to conduct arc discharge studies. The ten inch inner diameter and ability to monitor the temperature of the chamber mean the chamber is capable of working with the high temperatures expected with an arc. Minor changes to the electrical circuit of the glow discharge used in this experiment are needed as seen in Fig. 4.2.

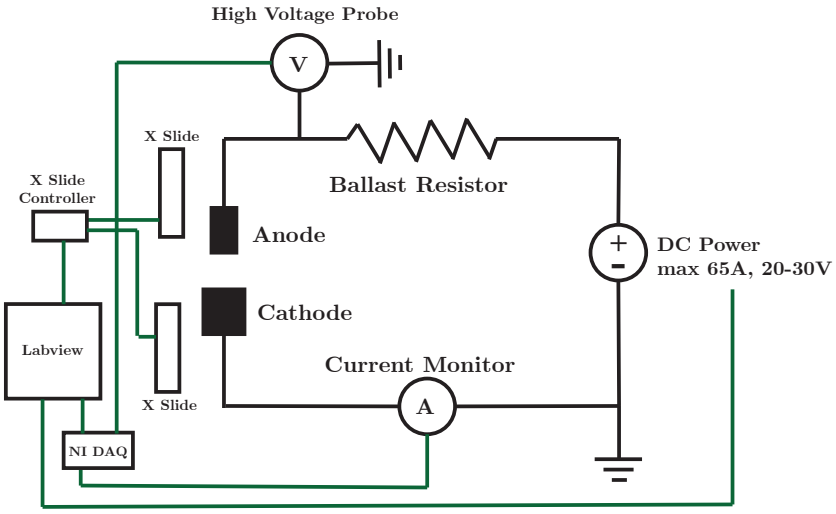

Figure 4.2: Electrical schematic for the arc discharge configuration. The ballast resistor will be approximately 0.2Ω.

Instead of the high voltages and low currents present in the glow, the arc is expected to produce voltages of approximately 20-30 V while current will be 30-40 A [90, 88, 89]. Due to the lower voltage, a lower ballast resistor is also needed. The large copper discs must be replaced with narrow graphite rods however the same translational stages may still be used.

REFERENCES

[1] X. Pan, P. Barker, A. Meschanov, J. Grinstead, M. Shneider, and R. Miles, "Temperature measurements by coherent Rayleigh scattering," *Optics Letters*, vol. 27, 2002.

[2] A. Gerakis, *Controlling and probing molecular motion with optical lattices*. PhD thesis, UCL (University College London), London, UK, 2014.

[3] A. Gerakis, M. Shneider, and B. Stratton, "Remote-sensing gas measurements with coherent Rayleigh-Brillouin scattering," *Applied Physics Letters*, vol. 109, 2016.

[4] O. Badran, "Gas-turbine performance improvements," in *Applied Energy*, vol. 64, 1999.

[5] D. Estruch, N. Lawson, and K. Garry, "Application of optical measurement techniques to supersonic and hypersonic aerospace flows," *Journal of Aerospace Engineering*, vol. 22, 2009.

[6] R. Hofer, *Development and Characterization of High-Efficiency, High-Specific Impulse Xenon Hall Thrusters*. PhD thesis, University of Michigan, Ann Arbor, MI.

[7] F. Xing, Y. Huang, M. Zhao, and J. Zhao, "The brief introduction of different laser diagnostics methods used in aeroengine combustion research," *Journal of Sensors*, vol. 2016, 2016.

[8] S. Wissel, A. Zwicker, J. Ross, and S. Gershman, "The use of dc glow discharges as undergraduate educational tools," *American Journal of Physics*, vol. 81, 2013.

[9] A. Schetnikov, "Euclid. optics," *Schole*, vol. 13, 2019.

[10] S. Trépanier, "Empedocles, on nature 1.273-287: Place, the elements, and still no 'we'," *Mnemosyne*, vol. 70, 2017.

[11] E. Slowik, "Descartes' physics," in *The Stanford Encyclopedia of Philosophy* (E. N. Zalta, ed.), Metaphysics Research Lab, Stanford University, fall 2017 ed., 2017.

[12] I. Newton and G. Hemming, *Opticks: or, A treatise of the reflections, refractions, inflexions and colours of light : also two treatises of the species and magnitude of curvilinear figures*. Printed for Sam. Smith, and Benj. Walford, 1704.

[13] H. Römer, *A Short Survey of the History of Optics*. New York, NY: Wiley, 2005.

[14] B. Walker, *Optical Engineering Fundamentals, Second Edition*. Bellingham, WA: SPIE, 2009.

[15] D. Lindberg, "Physico-mathesis de lumine, coloribus, et iride . francesco maria grimaldi," *Isis*, vol. 60, 1969.

[16] C. Huyghens, "Traité de la lumière," *Journal of the Röntgen Society*, vol. 16, 1920.

[17] A. McClelland and M. Mankin, *Young's Double Slit Experiment*. Cambridge, MA: Cambridge University Press, 2018.

[18] A.-J. Fresnel, "III. on the law of the partial polarization of light by reflexion," *Philosophical Transactions of the Royal Society of London*, vol. 120, 1830.

[19] H. Brittain, *Electromagnetic radiation and spectroscopy*. Boca Raton, FL: CRC Press, 2006.

[20] M. Al-Amri, M. El-Gomati, and M. S. Zubairy, *Optics in our time*. Basingstoke, UK: Springer Nature, 2016.

[21] J. Maxwell, "XXV. on physical lines of force," *The London, Edinburgh, and Dublin Philosophical Magazine and Journal of Science*, vol. 21, 1861.

[22] J. Maxwell, "A treatise on electricity and magnetism," *Nature*, vol. 7, 1873.

[23] J. Maxwell, "VIII. a dynamical theory of the electromagnetic field," *Philosophical Transactions of the Royal Society of London*, vol. 155, 1865.

[24] F. Kirchner, "Determination of the velocity of light from electromagnetic measurements according to W. Weber and R. Kohlrausch," *American Journal of Physics*, vol. 25, 1957.

[25] T. Simpson, "On Hertz and the speed of light," in *2017 IEEE Antennas and Propagation Society International Symposium, Proceedings*, vol. 2017-January, 2017.

[26] M. Jackson, "Fraunhofer and his spectral lines," *Annalen der Physik*, vol. 526, 2014.

[27] M. Planck, *On the Theory of the Energy Distribution Law of the Normal Spectrum*. 1967.

[28] M. Planck, "Ueber das gesetz der energieverteilung im normalspectrum (on the law of distribution of energy in the normal spectrum)," *Annalen der Physik*, vol. 309, 1901.

[29] A. Arons, "On a heuristic viewpoint concerning the production and transformation of light," *American Journal of Physics*, vol. 33, 1965.

[30] H. Hertz, "Ueber einen einfluss des ultravioletten lichtes auf die electrische entladung," *Annalen der Physik*, vol. 267, 1887.

[31] D. Siegel, "The collected papers of Albert Einstein.," *Isis; an international review devoted to the history of science and its cultural influences*, vol. 98, 2007.

[32] J. Tyndall, "XXXIII. on cometary theory," *The London, Edinburgh, and Dublin Philosophical Magazine and Journal of Science*, vol. 37, 1869.

[33] J. Gooch, *Tyndall Effect*. New York, NY: Springer, 2011.

[34] J. Howard, "John William Strutt, third Baron Rayleigh," *Applied Optics*, vol. 3, 1964.

[35] Rayleigh, "The late Lord Rayleigh's scientific papers," *Nature*, vol. 113, 1924.

[36] G. Mie, "Beiträge zur optik trüber medien, speziell kolloidaler metallösungen," *Annalen der Physik*, vol. 330, 1908.

[37] L. Brillouin, "Diffusion de la lumière et des rayons x par un corps transparent homogène," *Annales de Physique*, vol. 9, 1922.

[38] B. Guenther and D. Steel, *Encyclopedia of modern optics*, vol. 1-5. Amsterdam, Netherlands: Elsevier, 2018.

[39] C. Raman, "A new radiation," *Proceedings of the Indian Academy of Sciences - Section A*, vol. 37, 1953.

[40] R. Hinde, "Quantum chemistry, 5th edition (by Ira N. Levine)," *Journal of Chemical Education*, vol. 77, 2000.

[41] A. Schawlow and C. Townes, "Infrared and optical masers," *Physical Review*, vol. 112, 1958.

[42] T. Maiman, "Optical and microwave-optical experiments in ruby," *Physical Review Letters*, vol. 4, 1960.

[43] T. Maiman, "Stimulated optical radiation in ruby," *Nature*, vol. 187, 1960.

[44] R. Paschotta, *Field Guide to Lasers*. Bellingham, WA: SPIE, 2009.

[45] A. Dogariu, L. Dogariu, M. Smith, J. Lafferty, and R. Miles, "Single shot temperature measurements using coherent anti-Stokes Raman scattering in Mach 14 flow at the hypervelocity aedc tunnel 9," in *AIAA Scitech 2019 Forum*, 2019.

[46] D. Pulford, D. Newman, A. Houwing, and R. Sandeman, "The application of coherent anti-Stokes Raman scattering to temperature measurements in a pulsed high enthalpy supersonic flow," *Shock Waves*, vol. 4, 1994.

[47] M. Smith, O. Jarrett, R. Antcliff, B. Northam, A. Cutler, and D. Taylor, "Coherent anti-Stokes Raman spectroscopy temperature measurements in a hydrogen-fueled supersonic combustor," *Journal of Propulsion and Power*, vol. 9, 1993.

[48] F. Grisch, P. Bouchardy, V. Joly, C. Marmignon, U. Koch, and A. Gülhan, "Coherent anti-Stokes Raman scattering measurements and computational modeling of nonequilibrium flow," *AIAA journal*, vol. 38, 2000.

[49] R. Hancock, K. Boyack, and P. Hedman, *Coherent Anti-Stokes Raman Spectroscopy (CARS) in Pulverized Coal Flames*. Boston, MA: Springer, 1992.

[50] N. Deluca, R. Miles, W. Kulatilaka, N. Jiang, and J. Gord, "Femtosecond laser electronic excitation tagging (FLEET) fundamental pulse energy and spectral response," in *AIAA AVIATION 2014 - 30th AIAA Aerodynamic Measurement Technology and Ground Testing Conference*, 2014.

[51] J. Fisher, B. Chynoweth, M. Smyser, A. Webb, M. Slipchenko, J. Jewell, T. Meyer, and S. Beresh, "Femtosecond laser electronic excitation tagging velocimetry in a Mach six quiet tunnel," *AIAA Journal*, vol. 59, 2021.

[52] D. Zhang, B. Li, Q. Gao, and Z. Li, "Applicability of femtosecond laser electronic excitation tagging in combustion flow field velocity measurements," *Applied Spectroscopy*, vol. 72, 2018.

[53] L. Dogariu, A. Dogariu, R. Miles, M. Smith, and E. Marineau, "Femtosecond laser electronic excitation tagging velocimetry in a large-scale hypersonic facility," *AIAA Journal*, vol. 57, 2019.

[54] D. Walker, R. Williams, and P. Ewart, "Thermal grating velocimetry," *Optics Letters*, vol. 23, 1998.

[55] D. Zahradka, N. Parziale, M. Smith, and E. Marineau, "Krypton tagging velocimetry in a turbulent Mach 2.7 boundary layer," *Experiments in Fluids*, vol. 57, 2016.

[56] G. Wang, C. Jin, A. T. Le, and C. Lin, "Conditions for extracting photoionization cross sections from laser-induced high-order-harmonic spectra," *Physical Review A - Atomic, Molecular, and Optical Physics*, vol. 86, 2012.

[57] N. Parziale, M. Smith, and E. Marineau, "Krypton tagging velocimetry for use in high-speed ground-test facilities," in *53rd AIAA Aerospace Sciences Meeting*, 2015.

[58] D. Rothamer and R. Hanson, "Temperature and pressure imaging using infrared planar laser-induced fluorescence," *Applied Optics*, vol. 49, 2010.

[59] J. Seitzman, G. Kychakoff, and R. Hanson, "Instantaneous temperature field measurements using planar laser-induced fluorescence," *Optics Letters*, vol. 10, 1985.

[60] J. Seitzman, R. Hanson, P. DeBarber, and C. Hess, "Application of quantitative two-line oh planar laser-induced fluorescence for temporally resolved planar thermometry in reacting flows," *Applied Optics*, vol. 33, 1994.

[61] I. Grant, "Particle image velocimetry: A review," *Proceedings of the Institution of Mechanical Engineers, Part C: Journal of Mechanical Engineering Science*, vol. 211, 1997.

[62] L. Ukeiley, C. Tinney, R. Mann, and M. Glauser, "Spatial correlations in a transonic jet," *AIAA Journal*, vol. 45, 2007.

[63] A. Hsu, R. Srinivasan, R. Bowersox, and S. North, "Molecular tagging using vibrationally excited nitric oxide in an underexpanded jet flowfield," *AIAA Journal*, vol. 47, 2009.

[64] R. Sánchez-González, R. Srinivasan, R. Bowersox, and S. North, "Simultaneous velocity and temperature measurements in gaseous flow fields using the venom technique," *Optics Letters*, vol. 36, 2011.

[65] R. Sánchez-González, R. Bowersox, and S. North, "Vibrationally excited NO tagging by NO($A^2\sigma^+$) fluorescence and quenching for simultaneous velocimetry and thermometry in gaseous flows," *Optics Letters*, vol. 39, 2014.

[66] W. Tolles, J. Nibler, J. McDonald, and A. Harvey, "Review of the theory and application of coherent anti-Stokes Raman spectroscopy (CARS).," *Applied Spectroscopy*, vol. 31, 1977.

[67] A. P. Yalin, Y. Z. Ionikh, and R. B. Miles, "Gas temperature measurements in weakly ionized glow discharges with filtered rayleigh scattering," *Appl. Opt.*, vol. 41, no. 18, pp. 3753–3762, 2002.

[68] Q. Lao, P. Schoen, and B. Chu, "Rayleigh-Brillouin scattering of gases with internal relaxation," *The Journal of Chemical Physics*, vol. 64, 1976.

[69] R. Sandoval and R. Armstrong, "Rayleigh-Brillouin spectra in molecular nitrogen," *Physical Review A*, vol. 13, 1976.

[70] J. Grinstead and P. Barker, "Coherent Rayleigh scattering," *Physical Review Letters*, vol. 85, 2000.

[71] X. Pan, M. Shneider, and R. Miles, "Coherent Rayleigh-Brillouin scattering in molecular gases," *Physical Review A - Atomic, Molecular, and Optical Physics*, vol. 69, 2004.

[72] A. Gerakis, M. Shneider, and P. Barker, "Single-shot coherent Rayleigh–Brillouin scattering using a chirped optical lattice," *Optics Letters*, vol. 38, 2013.

[73] B. Finn, "Laplace and the speed of sound," *Isis*, vol. 55, 1964.

[74] A. Gerakis, J. Bak, and R. Randolph, "Dual color single-shot CRBS." 2021. Manuscript in Preparation.

[75] J. Bak, R. Randolph, and A. Gerakis, "Temperature and gas measurements in dual color CRBS." 2021. Manuscript in Preparation.

[76] A. Gerakis and M. Shneider, "Towards single shot gas flow velocity and temperature measurements with coherent Rayleigh-Brillouin scattering," in *AIAA Scitech 2019 Forum*, 2019.

[77] A. Gerakis, M. Shneider, B. Stratton, and Y. Raitses, "An all-optical, in situ diagnostic for large molecule and nanoparticle detection," in *Synthesis and Photonics of Nanoscale Materials XIV*, vol. 10093, (Bellingham, WA), SPIE, 2017.

[78] K. Repasky, G. Switzer, and J. Carlsten, "Design and performance of a frequency chirped external cavity diode laser," *Review of Scientific Instruments*, vol. 73, 2002.

[79] M. Fee, K. Danzmann, and S. Chu, "Optical heterodyne measurement of pulsed lasers: Toward high-precision pulsed spectroscopy," *Physical Review A*, vol. 45, 1992.

[80] B. Cornella, S. Gimelshein, M. Shneider, T. Lilly, and A. Ketsdever, "Experimental and numerical analysis of narrowband coherent Rayleigh–Brillouin scattering in atomic and molecular species," *Optics Express*, vol. 20, 2012.

[81] F. Chen, *Introduction to Plasma Physics and Controlled Fusion*. Los Angeles, CA: Springer, 3rd ed., 2016.

[82] V. Lisovskiy, H. Krol, and S. Dudin, "Investigation of dc glow discharge in CO2 using optical emission spectroscopy," *Problems of Atomic Science and Technology*, vol. 118, 2018.

[83] D. Ogle and G. Woolsey, "Diffuse and constricted glow discharges in SF6," *Journal of Physics D: Applied Physics*, vol. 20, 1987.

[84] L. Conde, *An introduction to plasma physics and its space applications, Volume 2: Basic equations and applications*. Bristol, UK: IOP Publishing, 2020.

[85] D. Xiao, *Fundamental Theory of Townsend Discharge*. Berlin, Heidelberg: Springer, 2016.

[86] J. T. Gudmundsson and A. Hecimovic, "Foundations of dc plasma sources," *Plasma Sources Science and Technology*, vol. 26, p. 123001, 11 2017.

[87] B. Wheaton, *Compendium of Quantum Physics*. Berlin, Heidelberg: Springer, 2009.

[88] S. Yatom, J. Bak, A. Khrabryi, and Y. Raitses, "Detection of nanoparticles in carbon arc discharge with laser-induced incandescence," *Carbon*, vol. 117, 2017.

[89] S. Yatom, A. Khrabry, J. Mitrani, A. Khodak, I. Kaganovich, V. Vekselman, B. Stratton, and Y. Raitses, "Synthesis of nanoparticles in carbon arc: Measurements and modeling," *MRS Communications*, vol. 8, 2018.

[90] Y. W. Yeh, Y. Raitses, and N. Yao, "Structural variations of the cathode deposit in the carbon arc," *Carbon*, vol. 105, 2016.